

RESEARCH ARTICLE

Analysis of defect mechanisms in nonstoichiometric ceria–zirconia by the microwave cavity perturbation method

Carsten Steiner¹  | Gunter Hagen¹ | Iurii Kogut² | Holger Fritze² | Ralf Moos¹ 

¹Department of Functional Materials, University of Bayreuth, Bayreuth, Germany

²Institute of Energy Research and Physical Technologies, Clausthal University of Technology, Goslar, Germany

Correspondence

Carsten Steiner, Department of Functional Materials, University of Bayreuth, 95440 Bayreuth, Germany.
Email: functional.materials@uni-bayreuth.de

Funding information

Deutsche Forschungsgemeinschaft, Grant/Award Numbers: MO 1060/29-1, FR 1301/23-1

Abstract

In this microwave study, the defect chemistry of ceria–zirconia solid solutions (CZO, $\text{Ce}_{1-y}\text{Zr}_y\text{O}_{2-\delta}$) was investigated at high temperatures by a resonant microwave method. Specifically, the effects of temperature and Zr content on the dielectric properties and defect chemistry mechanisms in CZO were analyzed. Experiments were performed on a series of different CZO powders ($y = 0.2, 0.33, 0.50, 0.67$). Measurements at 600°C and different oxygen partial pressures ($p_{\text{O}_2} = 10^{-26}$ –0.2 bar) confirm a dominant n -type conduction of small-polarons in CZO due to the preferred formation of oxygen vacancies, which is also supported by a multimodal analysis. Polarization losses were found to be negligible in the GHz range. Furthermore, an increased relative permittivity was observed in CZO, which correlates with the concentration of oxygen vacancies in CZO. Our microwave study is the first to provide a comprehensive data set for the dielectric properties of CZO powder sample in a wide range of different conditions. In addition, the connection of dielectric properties to CZO defect chemistry mechanisms is presented. The results are in good agreement with findings in the literature and may contribute to a better understanding of microwave-based state diagnosis of CZO-based materials, as it discussed for three-way catalysts.

KEYWORDS

ceria, defect chemistry, dielectric properties, exhaust gas aftertreatment, oxygen vacancies, quality factor, resonant frequency, small polaron hopping mechanism

1 | INTRODUCTION

Ceria and its solid solutions are indispensable for many modern applications and industrial processes. Applications range from synthesis gas generation,^{1–3} automotive catalysts,^{4–7} and catalytically active coatings^{8,9} to electrolyte materials for solid oxide fuel cells (SOFCs),^{10–15} and electrode materials for supercapacitors.^{16,17} Of key

importance in this context is the ability of ceria to reversibly release and incorporate oxygen in the lattice. The oxygen non-stoichiometry δ in ceria ($\text{CeO}_{2-\delta}$) is a result of the formation of oxygen vacancies (oxygen defects) in the crystal system.^{18–20} Depending on the application, these defect chemical properties can be influenced by the addition of different dopants. In the case of three-way catalysts (TWCs), for example, a

This is an open access article under the terms of the [Creative Commons Attribution-NonCommercial](https://creativecommons.org/licenses/by-nc/4.0/) License, which permits use, distribution and reproduction in any medium, provided the original work is properly cited and is not used for commercial purposes.

© 2022 The Authors. *Journal of the American Ceramic Society* published by Wiley Periodicals LLC on behalf of American Ceramic Society.

large oxygen storage capacity is desirable. The use of cerium–zirconium solid solutions (CZO, $\text{Ce}_{1-y}\text{Zr}_y\text{O}_{2-\delta}$) has proven to be especially successful, as they allow significantly higher non-stoichiometries under reducing conditions.^{21–23} Moreover, CZO exhibits higher thermal stability against sintering at high exhaust temperatures. This counteracts the loss of the high active surface area during operation and suppresses catalyst aging.^{24–27} CZO is also interesting as a component of electrodes for SOFC. In this context, composite anodes with a CZO layer exhibit high electrochemical activity and good reforming properties at the same time.²⁸ In addition, ceria-based solid electrolytes are subject of current research as they can be operated at significantly lower temperatures (500–800°C) compared to the commonly used yttria-stabilized zirconia.^{14,29–32} Due to its importance and the potential for future applications, the CZO material system and its redox behavior have been investigated intensively in the past decades, mostly with measurements of the electrical conductivity of bulk samples and thin films.^{21–23,33–35} Numerical methods are also increasingly used.^{36,37}

Dietrich et al. introduced an investigation method that allows the in situ determination of the dielectric properties of (catalytically active) powder samples using microwaves under typical operating conditions.³⁸ For that, a sample is placed inside a microwave cavity resonator in which an electromagnetic field in the GHz range is excited. According to the microwave cavity perturbation (MCP) theory,^{39–41} the dielectric properties of the samples inside of the cavity can be determined. In addition to ohmic losses due to free charge carriers (conductivity), polarization losses in the electromagnetic field can be measured. Furthermore, the method also provides information about the polarization capability (permittivity) of the samples.⁴⁰ In a recent study, the microwave properties as well as the defect chemistry of pure ceria could already be analyzed. Consistent with findings from other studies, a significant influence of the microstructure on the concentration of oxygen vacancies was found for nanocrystalline ceria.^{42,43} Another study also demonstrated the importance of Pt on the reducibility of pure ceria, especially at low temperatures.⁴⁴ Based on this study, an investigation of CZO used for a variety of technical application should provide further information on the defect chemical behavior under typical operating conditions. Moreover, the findings on the correlation of defect chemical and dielectric properties of ceria and CZO are of interest for the microwave-based status diagnosis of both catalysts and catalytically coated filter systems.^{45,46} As past studies have shown, the oxygen storage level of a TWC can also be determined *operando* using the MCP method.^{47–49} By using different high-frequency parameters, the diagnosis

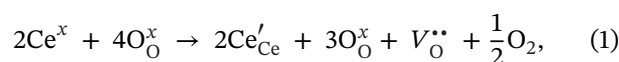
of the oxygen storage state is possible in a wide temperature range.⁵⁰ Monitoring and evaluation of catalyst aging is also possible.⁴⁸ Even dispensing with the usually applied oxygen (λ) probes would be feasible.^{51,52}

Therefore, in contrast to previous microwave studies, the experiments in this study focus on investigating the correlation of dielectric properties and defect chemistry especially of CZO. The experiments will help to better understand the defect and transport mechanisms in the oxygen storage and electrolyte material CZO and, also, to gain further information for optimizing the microwave-based state diagnosis of TWCs. In a first series of experiments, the influence of Zr^{4+} addition on the kinetics of oxygen transport in CZO is therefore investigated. For this purpose, the dielectric properties of $\text{Ce}_{1-y}\text{Zr}_y\text{O}_{2-\delta}$ ($y = 0.20, 0.33, 0.50, \text{ and } 0.67$) are investigated in the microwave resonator using a temperature ramp up to 600°C. Another experiment is then used to analyze the dielectric properties of CZO at different oxygen partial pressures at a constant temperature of 600°C. As part of the investigations, conductivities are determined from the obtained microwave data set, which are compared with measurement results from other studies. Of particular interest is a comparison to a previous study that analyzed sintered CZO ceramics and coatings using the same material as it is used here.^{43,52} A comparison to the microwave behavior of pure ceria is also given.⁴² The objective of this study is to obtain a data set for the dielectric properties of CZO. The comparison with conductivity data from literature and the dependences on temperature and oxygen partial pressure, conclusions can be drawn about the defect mechanisms in CZO. The dielectric properties are also analyzed with respect to the Zr content, and the effect of Zr on the defect mechanisms in CZO will be examined. The data set of the dielectric properties of CZO is also of importance for the microwave-assisted state diagnosis of automotive catalyst with CZO-based oxygen storage material.

2 | MATERIALS AND METHODS

2.1 | Defect chemistry of ceria–zirconia solid solutions

As with pure ceria, the defect chemistry of CZO is based on the formation of oxygen vacancies in the lattice, which is accompanied by the reduction of Ce^{4+} to Ce^{3+} cations^{21,22,36,53–56}:



with the cerium cations Ce^x_{Ce} (Ce^{4+}) and Ce'_{Ce} (Ce^{3+}), and the oxygen anions O_O^x (O^{2-}), the doubly positively

charged oxygen vacancies $V_{\text{O}}^{\bullet\bullet}$ in the lattice, and the free gaseous oxygen O_2 . The additional electrons at Ce^{3+} are bound to the cations and determine the electronic conductivity in the material due to the small polaron (hopping) mechanism.^{21,22} With non-stoichiometry, the electrical conductivity and thus the ohmic losses in CZO increase significantly. For the relationship between the density of conducting electrons n , respectively, the concentration of reduced cerium ions $[\text{Ce}'_{\text{Ce}}]$, and the oxygen vacancy concentration, the following electroneutrality condition holds^{21–23,57}:

$$n = [\text{Ce}'_{\text{Ce}}] = 2 [V_{\text{O}}^{\bullet\bullet}]. \quad (2)$$

The formation of oxygen vacancies generally occurs at high temperatures and low oxygen partial pressures. In CZO, the exchange of Zr^{4+} on Ce^{4+} lattice sites additionally leads to strain in the crystal.^{58–60} As a sevenfold coordination is energetically favored in the vicinity of the much smaller Zr^{4+} cations ($r_{\text{Zr}} = 0.98 \text{ \AA}$) compared to the typical eightfold coordination at the Ce^{4+} ions ($r_{\text{Ce}} = 1.11 \text{ \AA}$), the strain acts as an additional driving force for oxygen vacancy formation due to the so-called size effect. Therefore, CZO exhibits significantly higher oxygen vacancy concentrations than pure ceria under the same conditions.^{58–60} For the electrical conductivity in CZO, a $p_{\text{O}_2}^m$ -dependence of $m = -1/6$ is observed at low non-stoichiometries ($[\text{Ce}^{3+}] \ll [\text{Ce}^{4+}]$).²¹ Additionally, as the vacancy concentration increases, the interactions between the defects can also occur. In recent studies, they are attributed to associations between the differently charged Ce'_{Ce} and $V_{\text{O}}^{\bullet\bullet}$. In particular, dimers $(\text{Ce}'_{\text{Ce}} - V_{\text{O}}^{\bullet\bullet})^{\bullet}$ and trimers $(\text{Ce}'_{\text{Ce}} - V_{\text{O}}^{\bullet\bullet} - \text{Ce}'_{\text{Ce}})^x$ are of interest.^{57,61–65} For both, dimers and trimers, stronger $p_{\text{O}_2}^m$ -dependencies are to be expected according to the theoretical models. For dimers, the values are $m = -1/4$, for trimers even $m = -1/2$.^{21,62,63,65} An increase in m has also been observed experimentally in several studies.^{57,66,67}

At high temperatures and very low p_{O_2} , the non-stoichiometry in CZO can become so large that Ce^{4+} and Ce^{3+} cations are present in similar concentrations ($[\text{Ce}^{3+}] \approx [\text{Ce}^{4+}]$). In this case, the conductivity σ in CZO barely increases with higher non-stoichiometries and even passes through a maximum at $[\text{Ce}^{3+}] = [\text{Ce}^{4+}]$. The decrease in conductivity at even lower p_{O_2} has also been demonstrated in CZO in various studies.^{21,56,43} In contrast to CZO, this effect is observed in pure ceria only at very high temperatures and extremely low p_{O_2} .⁵⁶

In addition to the partial reduction of CZO (Equation 1), the number of extrinsic acceptor impurities is also crucial for the formation of oxygen vacancies. The incorporation of trivalent cations (e.g., Y^{3+} etc.) leads to additional oxygen vacancies^{18,21}:



with negatively charged acceptor cations A'_{Ce} . A similar effect can be observed for divalent cations (Ca^{2+} etc.). Especially at low non-stoichiometries (high p_{O_2} , low temperatures), extrinsically induced oxygen vacancies dominate in CZO. In these cases, the oxygen vacancy concentration is fixed by the acceptor concentration²¹:

$$[\text{A}'_{\text{Ce}}] = 2 [V_{\text{O}}^{\bullet\bullet}]. \quad (4)$$

According to the defect chemistry, a $p_{\text{O}_2}^m$ -dependence of the conductivity of $m = -1/4$ is then expected. As the incorporation of Zr^{4+} cations in CZO generally promotes the formation of oxygen vacancies, CZO can be described as a pure n -type conductor in most cases.^{33–35,43} Depending on the ambient conditions (T , p_{O_2}), the conduction electrons stem from oxygen vacancies of intrinsic and/or extrinsic origin. In contrast, ionic conductivity due to oxygen ions plays only a minor role for CZO compared to electronic conduction. However, for a high Zr content y in $\text{Ce}_{1-y}\text{Zr}_y\text{O}_{2-\delta}$ ($y > 0.50$), ionic conductivity can also contribute significantly to the overall conductivity at low non-stoichiometries δ (high p_{O_2}). In this case, the total CZO conductivity does not depend on the ambient p_{O_2} .³³ In literature, this is explained by the lattice distortion due to the smaller Zr^{4+} cations, which is largest for $0.20 < y < 0.50$.²³ For $y > 0.50$, this distortion decreases again significantly, which also results in a significant decrease in the fraction of electronic conductivity due to induced vacancies.³³

For pure ceria, it is also known that the microstructure and the active surface have a significant influence on the defect concentrations and on the electrical properties. Significantly higher conductivities have been found for nanocrystalline samples than for sintered ceramics.^{68–70} In literature, this effect is attributed to a decrease in the activation energy for the formation of oxygen defects on the surfaces, which is accompanied by the formation of space charge zones.^{68,71–74} However, the influence of grain size plays only a minor role in CZO. In various studies, Zr has been shown to be the dominant factor for the formation of oxygen vacancies in CZO due to the resulting lattice strain,^{21,22,33,35} similar to doped ceria.^{75,76}

2.2 | Preparation and sample characterization

The $\text{Ce}_{1-y}\text{Zr}_y\text{O}_{2-\delta}$ -powders were prepared by solid-state synthesis. For this purpose, cerium(IV)-oxide (chemPUR GmbH, 99.99% purity) and zirconium oxide powders (chemPUR GmbH, 99.95% purity, 2 wt.% Hf) were dried

at 120°C for at least 24 h and then weighed in stoichiometrically ($y = 0.20, 0.33, 0.50, \text{ and } 0.67$). The powders were mixed and homogenized in a planetary ball mill (Fritsch Pulverisette 5, Idar-Oberstein, Germany) in a ZrO_2 milling jar (stabilization: 3.5% MgO) with ZrO_2 milling balls ($\varnothing 10 \text{ mm}$, stabilization: 5.0% Y_2O_3). Homogenization was performed in two cycles of 2 min each at 400 rpm with a 15 min break between each cycle. The powder mixtures were then calcined in an alumina annealing box in a chamber furnace (Nabertherm LHT08/17 chamber furnace, Nabertherm GmbH, Lilienthal, Germany) at 1650°C for 12 h (heating rate: 5 K/min, cooling with furnace constant). Using the same equipment as for homogenization, the calcined powders were ground (nine cycles, 400 rpm, each 5, 15 min pause in between). As a final step, the powders were annealed at 623°C for 24 h in a chamber furnace to regenerate the oxygen deficiency (heating rate: 5 K/min). The results from the high-frequency tests in this study are also compared with experimental findings from other studies using sintered samples prepared from the same powders. The sintered samples were prepared by firing at 1650°C. For further details on the synthesis route, material properties, and contacting, we refer in this context to our former study.⁴³

The crystallographic structure of the powders was investigated by X-ray diffraction (XRD) (Bruker D8 Advance, Billerica, MA, USA) using a 2.2 kW Cu-anode and a $K_{\alpha 1}$ wavelength of 1.540 Å, germanium- $K_{\alpha 1}$ -monochromator and an energy-dispersive 1D-LYNXEYE detector in a range of $2\theta = (25^\circ - 75^\circ)$ and a resolution of 0.02°. For the analysis of the lattice properties, the diffraction patterns were evaluated using the Rietveld analysis (software: DIFFRAC.SUITE TOPAS). The morphology of the powders was also examined using a scanning electron microscope (SEM, Leo 1530 P V, Zeiss, Oberkochen, Germany). Possible impurities were also evaluated on the initial powders CeO_2 and ZrO_2 by laser-ablation-inductively coupled plasma-mass-spectroscopy (LA-ICP-MS, Element XR, ThermoScientific, Bremen, Germany). For ceria, the dominant impurities were found to be SiO_2 (450 ppm), Al_2O_3 (120 ppm), and CaO (80 ppm) and for ZrO_2 : SiO_2 (660 ppm), Al_2O_3 (512 ppm), CaO (100 ppm), and Fe_2O_3 (200 ppm). The concentration of other impurities (La_2O_3 , Y_2O_3 , etc.) was found to be below (<15 ppm) and is considered to negligible.

The particle size distributions of the CZO powders were determined by laser-diffraction (LD) (Mastersizer 2000, Malvern Instruments, Worcestershire, UK). For the investigation, the powders were previously dissolved in water with a wetting agent. Ultrasonic vibration was then used to break up loose agglomerates and to ensure a homogeneous particle distribution in the solution. The results of the material characterization, exemplarily for

the $\text{Ce}_{0.80}\text{Zr}_{0.20}\text{O}_2$ - and $\text{Ce}_{0.50}\text{Zr}_{0.50}\text{O}_2$ -powders, are shown in Figure 1. Part (A) shows the XRD diffraction pattern, (B) the morphology (SEM image) of the powder particles, and (C) the particle size distribution of $\text{Ce}_{0.80}\text{Zr}_{0.20}\text{O}_2$. Parts (D)–(F) contain the corresponding information for $\text{Ce}_{0.50}\text{Zr}_{0.50}\text{O}_2$. An overview of the crystallographic properties of each powder calculated from the Rietveld analysis is also given in Table 1.

As shown in Figure 1A, $\text{Ce}_{0.80}\text{Zr}_{0.20}\text{O}_2$ crystallizes in the typical cubic c -phase.^{23,33,77,79–81} As the SEM image (Figure 1B) indicates, the powder consists of both large grains with a size of several μm and a large number of smaller particles only a few tens of nm in size. This composition is also confirmed by LD (Figure 1C). Here, a bimodal particle size distribution is observed, with a dominating fraction of larger particles. The angular morphology of the particles in the SEM image (Figure 1B) is probably due to the fact that the coarse grains produced by the high temperatures during calcination were partially broken up and crushed by the mechanical stress in the subsequent milling process. Furthermore, according to the data from the Rietveld analysis of $\text{Ce}_{0.80}\text{Zr}_{0.20}\text{O}_2$ (Table 1), the polycrystalline powder has a crystallite size of about 150 nm and has lattice parameters consistent with those reported in other studies.^{23,77} Powders with more Zr show similar properties but differ in some details from $\text{Ce}_{0.80}\text{Zr}_{0.20}\text{O}_2$. In terms of crystal system, the $\text{Ce}_{0.67}\text{Zr}_{0.33}\text{O}_2$ -powder was also found to be cubic c -phase (Table 1). As past studies have shown, for example, with Raman spectroscopy, this could also be a pseudo-tetragonal (t'') crystal system, where only the oxygen ions show a slight elongation in the lattice.^{79,82} As both phases are hardly distinguishable in XRD measurements and, moreover, the defect chemical properties of the material remain unaffected,^{79,83} this detail will not be further investigated here. Powders with even higher Zr-content ($y = 0.50, 0.67$) crystallize in the (metastable) tetragonal phase (t'), as shown for $\text{Ce}_{0.50}\text{Zr}_{0.50}\text{O}_2$ in Figure 1D.^{79,80,84,85} Although the $\text{Ce}_{0.50}\text{Zr}_{0.50}\text{O}_2$ -powder could be synthesized in single-phase, small amounts of the stable t -phase are detectable in XRD patterns for $\text{Ce}_{0.33}\text{Zr}_{0.67}\text{O}_2$, due to the duration of the cooling process after calcination.⁸⁶ However, the amount of t -phase in $\text{Ce}_{0.33}\text{Zr}_{0.67}\text{O}_2$ is low and was estimated to be less than 4% by the Rietveld analysis.

Moreover, the morphology of all synthesized CZO powders is similar. Moreover, here a bimodal particle size distribution is observed via LD for powders with higher y , with the dominant fraction always consisting of larger grains of several microns in diameter (Figure 1E,F for $\text{Ce}_{0.50}\text{Zr}_{0.50}\text{O}_2$). A closer analysis of the particle size distribution also reveals that the proportion of smaller particles decrease with increasing Zr-concentration, as shown by the comparison of Figure 1C,F. Possibly, the incorporation

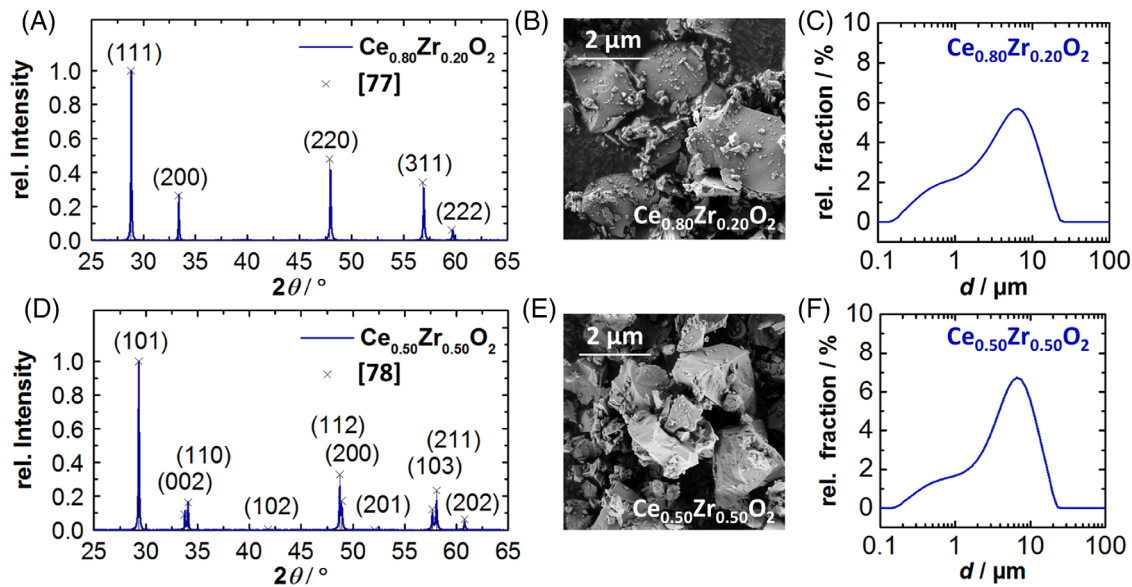


FIGURE 1 Material characterization of CZO powders: (A) X-ray diffraction (XRD) pattern,⁷⁷ (B) SEM image of the particles, (C) particle size distribution of $\text{Ce}_{0.80}\text{Zr}_{0.20}\text{O}_2$, and (D) XRD pattern,⁷⁸ (E) SEM image of the particles, (F) particle size distribution of $\text{Ce}_{0.50}\text{Zr}_{0.50}\text{O}_2$

TABLE 1 Lattice parameter und crystallite size of the CZO-powders calculated from Rietveld analysis

Powder	Phase	Lattice parameters a, b, c (Å)	Crystallite size (nm)	Residual fit error (%)
$\text{Ce}_{0.80}\text{Zr}_{0.20}\text{O}_2$	c	5.3585(6)	152.2	8.7
$\text{Ce}_{0.67}\text{Zr}_{0.33}\text{O}_2$	c (t'')	5.3246(10)	142.6	10.6
$\text{Ce}_{0.50}\text{Zr}_{0.50}\text{O}_2$	t'	5.3076(5) 3.7214(8)	136.2	9.7
$\text{Ce}_{0.33}\text{Zr}_{0.67}\text{O}_2$	t'	5.27115(9) 3.6821(15)	139.9	11.7

Note: The numbers in brackets represent the uncertainties in the last digits of the lattice parameters.

of Zr increases the mechanical stability of CZO, resulting in powders with high Zr content being less crushed during milling. The Rietveld analysis also demonstrates similar crystallite sizes in the 100 nm range.

Overall, the powders prepared by solid-state synthesis show the typical phase distribution of CZO. Similarly, observations on morphology and microstructure are in agreement with experiences from literature.^{79,81,83,85} Thus, synthesized materials provide a solid foundation for studying the dielectric and defect properties of CZO.

2.3 | MCP-fundamentals

The MCP method is a contactless measurement technique, commonly used for the dielectrical material characterization. In general, samples have the complex permittivity $\epsilon^{39,40}$:

$$\begin{aligned} \epsilon &= \epsilon' - j \epsilon'' = \epsilon_0(\epsilon'_r - j \epsilon''_r) \\ &= \epsilon_0 \left(\epsilon'_r - j \left(\epsilon''_{\text{Pol}} + \frac{\sigma}{2\pi f \epsilon_0} \right) \right). \end{aligned} \quad (5)$$

The real part represents the permittivity of the ϵ' of the sample, which is composed of the relative permittivity of

the sample ϵ'_r and the electric field constant of the vacuum ϵ_0 . The imaginary part represents the dielectric loss ϵ'' within the sample, which is analogously associated with the relative dielectric loss ϵ''_r . The dielectric loss includes losses from the polarization of the material (ϵ''_{Pol}) and ohmic losses from the conductivity σ . In theory, both contributions are frequency dependent—especially for the conductivity, there is an inverse proportionality to the measurement frequency f .

A cylindrical cavity resonator (aluminum, \varnothing 184 mm, height $h_C = 80$ mm) is applied for the dielectric characterization of CZO. It uses the TM_{010} resonant mode and its higher modes (TM_{020} , TM_{030}). The typical resonant frequencies are $f_{\text{TM}010} \approx 1.18$ GHz, $f_{\text{TM}020} \approx 2.62$ GHz, and $f_{\text{TM}030} \approx 4.18$ GHz. Three quartz tubes with different diameters are arranged concentrically along the resonator axis. In the inner (sample) tube (\varnothing 10 mm), the sample is localized on a porous quartz frit. A sketch of the resonator setup is found in the [Supplementary Information](#) of this study. Through the frit, the sample is flushed with different process gases. Temperatures, typical for exhaust gas experiments, are provided by a heated air flow (approx. 50 l/min) between a second tube and the sample tube. A

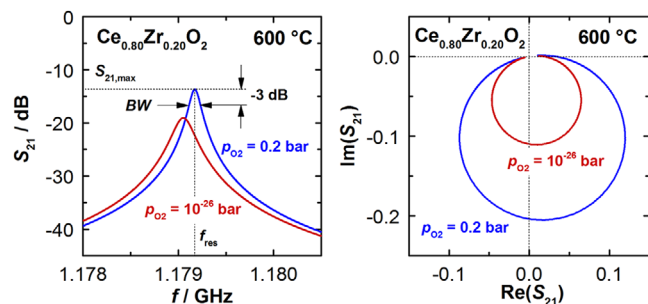


FIGURE 2 Microwave spectra at the TM_{010} mode for the $Ce_{0.80}Zr_{0.20}O_2$ -powder at $600^\circ C$ for high (0.2 bar) and low (10^{-26} bar) p_{O_2} : (A) transmitted power S_{21} (in dB), (B) resonant circle of the TM_{010} in the complex plane

vacuum-isolated area between the second and the outer, the third tube provides thermal isolation of the setup. With this arrangement, sample temperatures of up to $600^\circ C$ can be achieved. At the same time, the resonator itself is constantly cooled to $20^\circ C$ by water cooling. The temperature above and below the resonator is monitored by thermocouples. Further details on the design of the resonator and the concept of the resonator (including sketches) were also published earlier.³⁸

The electromagnetic coupling of the resonator is implemented by two loop antennas. They allow a measurement of the transmitted power. At discrete frequencies (resonances), standing electromagnetic waves are excited in the resonator, at which a maximum in the transmitted power S_{21} can be detected in the spectrum. As an example, Figure 2A shows the transmission spectrum (S_{21} in dB) near the TM_{010} mode for a $Ce_{0.80}Zr_{0.20}O_2$ -sample at $600^\circ C$. The resonances are characterized by the resonant frequency f_{res} , the half-bandwidth BW, and the maximum power amplitude $S_{21,max}$.^{39,87,88} The half-bandwidth is the dominant parameter for the quality factor of the resonance $Q = f_{res}/BW$. As can be seen in Figure 2A, these resonant parameters change with the dielectric properties of the sample. In general, a larger permittivity leads to lower resonant frequencies. The inverse quality factor $1/Q$ in turn correlates with the dielectric losses. Analogously to previous studies (also at TWC),^{41,50,89} the $Ce_{0.80}Zr_{0.20}O_2$ -sample typically exhibits higher resonant frequencies and, at the same time, lower attenuations at high oxygen partial pressures (blue) than at low p_{O_2} (red).

In the complex plane (Figure 2B), the S_{21} data points close to the resonance form a circle. The diameters of the resonant circles are correlated with the transmitted power of the mode S_{21} . In contrast, S_{21} data points, obtained from frequencies away from the resonance, can be found near the origin.^{40,90–92} For the determination of the resonant parameters in this study, squares root regression of the resonant circles is applied, as this method is considered

robust and accurate^{91,93} and has been successfully used in previous studies.^{41,44,42} Using MCP theory, the dielectric properties of a sample can be determined from the resonant parameters. The theory is based on the electric field perturbation caused by the insertion of a sample. Therefore, the changes of the resonant frequency and the quality factor are evaluated, which can be described by the following equations⁹⁰:

$$\epsilon_r' - 1 = \frac{V_C \frac{\Delta f}{f_0} \left(\frac{V_S V_C}{2V_{eff}} - N_e V_C \frac{\Delta f}{f_0} \right) - \frac{1}{4} N_e V_C^2 \left(\Delta \frac{1}{Q} \right)^2}{\left(\frac{V_S V_C}{2V_{eff}} - N_e V_C \frac{\Delta f}{f_0} \right)^2 + \frac{1}{4} (N_e V_C)^2 \left(\Delta \frac{1}{Q} \right)^2}, \quad (6)$$

$$\epsilon_r'' = \frac{\frac{1}{2} V_C \left(\Delta \frac{1}{Q} \right) \left(\frac{V_S V_C}{2V_{eff}} - N_e V_C \frac{\Delta f}{f_0} \right) - \frac{1}{2} N_e V_C^2 \frac{\Delta f}{f_0} \left(\Delta \frac{1}{Q} \right)}{\left(\frac{V_S V_C}{2V_{eff}} - N_e V_C \frac{\Delta f}{f_0} \right)^2 + \frac{1}{4} (N_e V_C)^2 \left(\Delta \frac{1}{Q} \right)^2}, \quad (7)$$

with the volume of the resonator V_C and the sample V_S , the modal effective volume V_{eff} of the mode and the effective depolarization factor N_e of these. The changes of the resonant parameters are defined as follows:

$$\frac{\Delta f}{f_0} = \frac{(f_0 - f_s)}{f_0}, \quad (8)$$

$$\Delta \left(\frac{1}{Q} \right) = \frac{1}{Q_{0,S}} - \frac{1}{Q_{0,0}}, \quad (9)$$

with the resonant frequency f_0 and the (unloaded) quality factor $Q_{0,0}$ of the resonator without sample and the corresponding resonant parameters f_0 and $Q_{0,S}$ of the resonator with sample. The modal volume was determined analogously to previous studies from simulations of the field distribution within the resonator. $V_{eff}/V_C = 26.78\%$ for the TM_{010} mode, $V_{eff}/V_C = 13.73\%$ for the TM_{020} mode, and $V_{eff}/V_C = 12.84\%$ for the TM_{030} mode were obtained. An impact on the resonance properties of the modes by interferences with other modes can also be excluded.⁴¹ As the samples in the resonator generally have a lower height (h_s) than the height of the resonator ($h_s < h_C$), additional field weakening is observed due to depolarization within the sample geometry. This effect is mainly affected by the sample geometry and the orientation of the sample in the electric field. The field weakening of the excitation field is typically described by the dimensionless effective depolarization factor N_e .^{94–96}

CZO powder samples with a mass of $m_s = 0.35$ g were investigated in the study. The relative bulk densities of the samples are shown in Table 2. With a porosity fraction of about 70%, the values are similar for all powder samples. Depolarization factors were determined for the bulk densities in the resonator (Table 2). The analytical

TABLE 2 Relative bulk density and effective depolarization factor of the CZO powder samples

Powder	Rel. bulk density ν_S (%)	Effective depolarization factor N_e
Ce _{0.80} Zr _{0.20} O ₂	32.4	0.389
Ce _{0.67} Zr _{0.33} O ₂	28.2	0.348
Ce _{0.50} Zr _{0.50} O ₂	31.4	0.395
Ce _{0.33} Zr _{0.67} O ₂	33.1	0.397

approach assumes a cylindrical sample geometry with its axis of symmetry aligned parallel to the field direction in the resonator.⁹⁴ The exact approach, as well as the assumptions and limitations made, are explained in detail in our previous study.⁴¹ The results of the calculation are shown in Table 2.

The comparison of the depolarization factors with the bulk densities shows that samples with lower bulk density also have lower depolarization factors. This effect is expected as samples with low bulk density occupy a larger volume in the resonator and consequently have a higher bulk height h_S . The effect of depolarization, in turn, decreases with h_S and N_e becomes zero when $h_S = h_C$. Compared to the study on pure ceria, the CZO powders have higher bulk densities ($\nu_{\text{CeO}_2} = 20.6\%$ ⁴²) and thus stronger a depolarization. This effect can be plausibly explained by the high calcination temperatures and the associated grain growth, which enhances the powders density and reduces the porosity.

Equations (6) and (7) can be used to determine the dielectric properties of the powders. Before this, however, the porosity must be taken into account in order to be able to derive the dielectric material parameters of the CZO material itself. In the case of ceria-based materials, the Looyenga mixing rule has been successfully applied several times^{42,41,97}:

$$(\epsilon)^k = \sum_i^n \nu_i (\epsilon_i)^k, \quad (10)$$

with the complex permittivity of the bulk ϵ , the volume fraction ν_i and the complex permittivity ϵ_i of the i -th constituent, and the mixing exponent $k = 1/3$ for Looyenga. The mixing model is especially suitable for homogeneous mixtures, such as powders (mixture of air and material),^{98,99} and gives good results even in the case of higher losses,^{100,101} which can also be expected in reducing conditions due to the CZO defect chemistry. Moreover, our experience and comparison with the literature confirm that the mixing model is a good choice for CZO materials.

2.4 | Experimental procedures

Our study uses two types of experiments for the dielectric characterization of CZO. Prior to the measurements, the powders were dried at 200°C for at least 24 h, to avoid the effect of possible water adsorption on the surface of the powders. The experiment is designed to analyze the reducibility and the kinetics of oxygen incorporation and release during heating. It also provides information about the effect of Zr on the temperature-dependent dielectric properties in CZO. Therefore, the oxidized CZO powders were heated to 600°C in the resonator with a continuous temperature ramp (1.5 K/min), which is shown in Figure 3A (black line). The procedure was performed a first time with synthetic air (20% O₂) and a second time under reducing conditions with 3.5% H₂ to observe the chemical reduction of CZO during the temperature ramp. Typical microwave signals (f_{res} (blue), Q_0^{-1} (red line)) during the experiment, which were obtained similarly in one of our previous studies,⁴² are shown in Figure 3A on the right axes (exemplarily for Ce_{0.80}Zr_{0.20}O₂). Additionally, a reference measurement of the resonator without sample is performed (Figure 3A, blue-dashed). From these changes of the resonance parameters to the reference measurement, the dielectric sample properties can be derived.

In analogy to the data of the previous study,⁴² the resonant frequency (Figure 3A) continuously decreases with temperature during the measurement due to the thermal expansion and increasing permittivity of the resonator structure (quartz tubes, etc.). The resonant frequencies of the measurements with powder (red and blue) proceed parallelly to the empty measurement (black-dashed) in this phase. The quality factor (Figure 3A) also barely changes at first. Only at very high temperatures (>500°C), the curves diverge increasingly between oxidizing and reducing conditions as a result of the formation of oxygen vacancies in CZO.

In another type of experiment, the dependence of the dielectric properties of CZO on the oxygen partial pressure at a constant temperature of 600°C is analyzed. By comparing the sample conductivities σ and their p_{O_2} -dependences, the data can clarify whether powders show similar defect chemical properties like sintered ceramics or films of the same material investigated in previous studies.^{43,52} Even though the electric conductivity of sintered CZO ceramics or coatings has been analyzed many times in the literature,^{33–35,52} to the best of our knowledge, no such studies dealing with powder samples are available. In addition, the experiment may provide information on the correlation of polarization and any polarization losses that may occur in CZO, which may further add to the previous understanding of CZO defect chemistry.

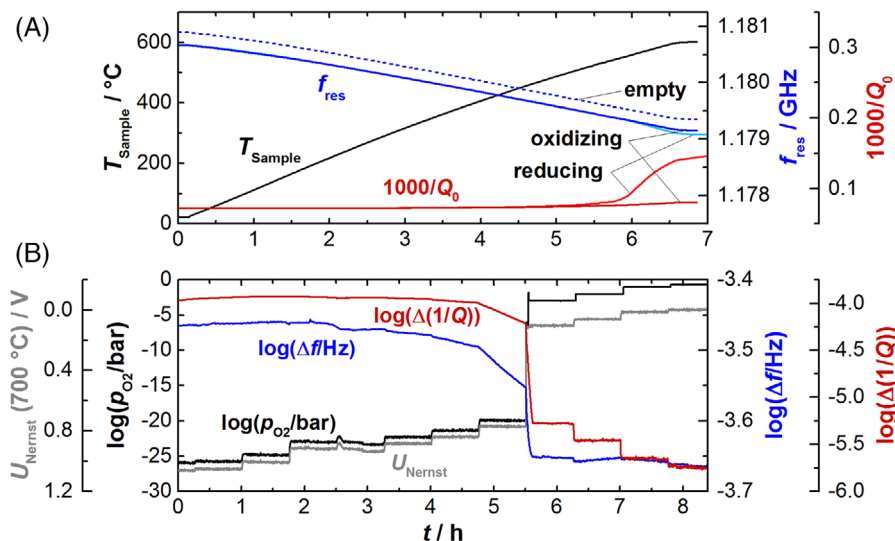


FIGURE 3 Microwave experiments for the dielectrical characterization (TM₀₁₀-data, Ce_{0.80}Zr_{0.20}O₂): (A) temperature ramp with f_{res} (dark blue) and Q_0^{-1} (red) under oxidizing (20% O₂) and reducing conditions (3.5% H₂, light blue, red, almost identical) and for the empty resonator (blue-dashed), (B) stepwise increasing p_{O_2} at 600°C with the logarithmic changes of f_{res} (blue) and Q_0^{-1} (red)

Before starting the experiment, the samples were reduced at 600°C in the resonator at low $p_{\text{O}_2} \approx 10^{-26}$ bar until the defect chemical equilibrium was established. Taking the Ce_{0.80}Zr_{0.20}O₂ powder as an example, the typical procedure of the experiment, including the changes in the resonant parameters, is shown in Figure 3B. High oxygen partial pressures (10^{-4} bar $\leq p_{\text{O}_2} \leq 0.2$ bar) are generated via O₂/N₂ mixtures using mass flow controllers. Low oxygen partial pressures (10^{-26} bar $\leq p_{\text{O}_2} \leq 10^{-19}$) are obtained by H₂/H₂O equilibria. The oxygen partial pressure was measured downstream of the resonator using a commercial Nernst cell of known temperature (BOSCH LSF 4.2, 700°C). Using the Nernst Equation (11) and the mass action law of the hydrogen–water reaction (12), the p_{O_2} at the sample location can be calculated, similar to other studies¹⁰²:

$$U_{\text{Nernst}} = \frac{RT}{4F} \ln \frac{p_{\text{O}_2}}{p_{\text{O}_2, \text{ref}}}, \quad (11)$$

$$K_{\text{H}_2\text{O}}(T) = \frac{[\text{H}_2] p_{\text{O}_2}^{0.5}}{[\text{H}_2\text{O}]}, \quad (12)$$

with the universal gas constant R , the Faraday constant F , the reference oxygen partial pressure $p_{\text{O}_2, \text{ref}} = 0.21$ bar, the temperature-dependent equilibrium constant $K_{\text{H}_2\text{O}}$, and the concentrations of hydrogen $[\text{H}_2]$ and water $[\text{H}_2\text{O}]$.

As shown by the measured Nernst voltage (Figure 3B, gray) and the calculated p_{O_2} (black) at the sample, the p_{O_2} increases gradually during the experiment. At $t \approx 5.5$ h, the transition from reducing to oxidizing conditions occurs. At the end ($t \approx 7.8$ h), the oxygen partial pressure is 0.21 bar. The (logarithmic) changes in the resonant frequency f_{res}

(blue) and the inverse quality factor Q^{-1} (red) are shown in Figure 3B. Both resonant parameters hardly react to changes in p_{O_2} at low p_{O_2} . Although this result was found similarly for the other CZO powders, this observation represents a fundamental difference compared to the results measured for pure ceria. There, a stepwise change of the resonant parameters and thus of the dielectric parameters with p_{O_2} was clearly detectable also under reducing conditions.⁴²

After the change to oxidizing conditions (Figure 3B, $t \approx 5.5$ h), especially the signal of the inverse quality factor Q^{-1} decreases further with each p_{O_2} -step. The change in the Q^{-1} signal throughout the experiment spans two orders of magnitude. Instead, only a small progressive decrease in resonant frequency is observed at high p_{O_2} , which is consistent with the results found for ceria.⁴² In summary, the fundamental behavior of CZO in the microwaves experiment is found to be similar to pure ceria; however, differences can be observed in certain detail. A deeper analysis with derived dielectric parameters and discussion of the defect chemical background will be given in the following chapter.

3 | RESULTS AND DISCUSSION

3.1 | Effect of temperature on the dielectric properties of CZO

In this section, the effect of temperature on CZO under reducing conditions is presented. First, we will consider the effect of Zr on polarization in the lattice ϵ_r' at room

TABLE 3 Relative Permittivity ϵ'_r of CZO at room temperature

Powder	ϵ'_r
CeO ₂	22.2 ⁴²
Ce _{0.80} Zr _{0.20} O ₂	24.5
Ce _{0.67} Zr _{0.33} O ₂	26.6
Ce _{0.50} Zr _{0.50} O ₂	27.4
Ce _{0.33} Zr _{0.67} O ₂	29.0

temperature, which is shown in Table 3. In addition, the value for pure ceria is also shown, adopted from Ref. [42]. Apparently, the replacement of Ce sites by Zr⁴⁺ ions leads to a slight increase in the relative permittivity. This result agrees with other studies that analyzed the dielectric properties of CZO by impedance spectroscopy or by DFT studies.^{103,104} The dielectric losses ϵ''_r are too small to be determined at room temperature.

Based on these values, the change in the dielectric properties at higher temperatures will be analyzed in the following. Of particular interest is the effect of Zr on the thermally activated reduction of CZO. Therefore, the dielectric properties of CZO powders are derived for oxidizing and reducing conditions from the microwave experiment (Figure 3A). Additionally, the change in dielectric properties due to chemical reduction is calculated by the following equation:

$$\Delta\epsilon'_r = \epsilon'_{r,\text{red}} - \epsilon'_{r,\text{oxi}}, \quad (13)$$

$$\Delta\epsilon''_r = \epsilon''_{r,\text{red}} - \epsilon''_{r,\text{oxi}}, \quad (14)$$

with the difference of the relative permittivity $\Delta\epsilon'_r$ and the dielectric loss $\Delta\epsilon''_r$, the relative permittivities $\epsilon'_{r,\text{red}}$ and $\epsilon'_{r,\text{oxi}}$ under reducing and oxidizing conditions, respectively, and the corresponding dielectric losses $\epsilon''_{r,\text{red}}$ and $\epsilon''_{r,\text{oxi}}$. Figure 4A,B shows these data, calculated from the TM₀₁₀ mode signal (≈ 1.18 GHz). Figure 4C,D includes the corresponding properties determined from the TM₀₂₀ signal (≈ 2.62 GHz). In addition to the results on CZO powders, data from pure ceria (from Ref. [42]) were also integrated into the diagram.

As can be seen, the properties under oxidizing and reducing conditions are similar over large parts of the experiment. Only at temperatures well above 500°C, the differences occur and increase with temperature. Then, under reducing condition, a continuous increase of both relative permittivity and of dielectric losses is observed. The latter is expected due to the thermally activated formation of oxygen vacancies and migration of electrons localized at the Ce³⁺-cations in CZO.^{34,35,33} Without going into detail about the underlying mechanisms at this point (details in Section 3.2), the focus of this investigation will

be on the differences between CZO powders. In addition, the results will be compared with the data of pure ceria.

Comparing the data of the different CZO powders with each other, we find that as the Zr-content y increases, so does the temperature at which the formation of oxygen vacancies in the material is first observed. Although the redox behavior in Ce_{0.80}Zr_{0.20}O₂ is detectable from a temperature of $T = 530^\circ\text{C}$, comparable changes in Ce_{0.33}Zr_{0.67}O₂ do not occur until $T = 570^\circ\text{C}$. Reduction in CZO therefore requires higher temperatures as the Zr-fraction y increases. The temperatures also differ significantly from those for pure ceria, where reduction was observed as early as $T = 480^\circ\text{C}$. Moreover, the chemical equilibrium (of the defects) was reached when the target temperature of 600°C was met.⁴² In the case of CZO, oxygen vacancy formation, or reduction, continued beyond the experiment. To evaluate this effect, the morphology must be considered at this point in addition to the kinetics of oxygen transport. Although the microstructure of the CZO powders is largely similar (Section 2.2), the ceria powder in particular exhibits smaller crystallites and grain sizes. Therefore, the differences in the behavior of the CZO powders most likely come from Zr itself, whereas the differences from pure ceria are also influenced by the microstructure. The calculated activation energy for the formation of oxygen vacancies of the ceria powder of $E_a = 1.03$ eV⁴² already indicated a large influence of the microstructure in this case.

It is also noticeable in the data that the signal amplitudes of the dielectric loss are consistently smaller for the higher resonant mode (TM₀₂₀) than for the basic mode (TM₀₁₀). This fact has already been observed in ceria and is further evidence that CZO losses are indeed from small polaron hopping (localized electrons), as smaller contributions from electronic conductivity to the dielectric losses at higher frequencies can be expected (according to Equation 5). Therefore, the CZO powders are likely primarily an n-type conductor, as has been confirmed many times in the literature^{33–35} including our measurements on sintered ceramics or PLD films.⁴³ In addition, proton conduction has also been observed in the literature in ceria and CZO, which arises from an interaction with hydrogen and water vapor at the surfaces, forming hydroxyl and hydride species. The effect is favored by samples with a high surface area (grain size: nm range) at low temperatures (200–350°C).¹⁰⁵ In our study, there is no evidence of significant contribution from proton conduction. Moreover, as the CZO particles are relatively large (μm -range, crystallite sizes > 100 nm) due to the solid-state reaction route of synthesis and the high experiment temperatures (600°C), a significant contribution seems unlikely in this study.

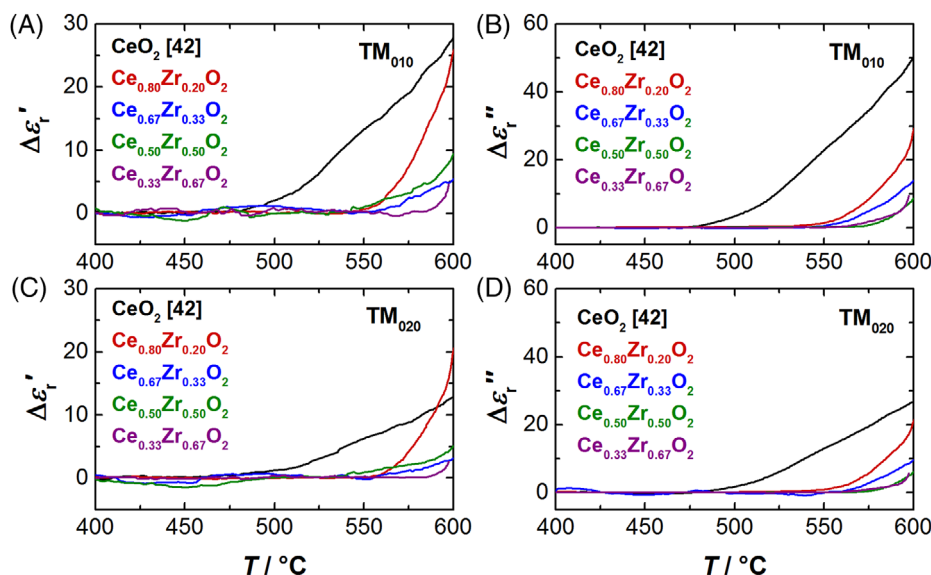


FIGURE 4 Difference of the dielectric parameters of CZO powders between heating under oxidizing (20% O₂) and reducing conditions (3.5% H₂): (A) of relative permittivity $\Delta\epsilon'_r$ and (B) dielectric loss $\Delta\epsilon''_r$ according to TM₀₁₀-signal (≈ 1.18 GHz); analogously (C and D) according to TM₀₂₀-signal (≈ 2.62 GHz). Included are data from CeO₂.⁴²

3.2 | RF-analysis of the CZO defect chemistry

In another experiment, the CZO powders were investigated at 600°C and different p_{O_2} values. Figure 5 demonstrates the correlation of the dielectric properties with p_{O_2} for all investigated CZO powders. In the figure, the left axes show the change in relative permittivity, $\Delta\epsilon'_r$, that represents the additional polarization occurring due to the formation of oxygen vacancies. Only this part of the permittivity is expected to be a function of the oxygen vacancy concentration, that is, the p_{O_2} . Accordingly, the part of the permittivity originating from the lattice itself ($\epsilon'_{r,L}$) is subtracted:

$$\Delta\epsilon'_r = \epsilon'_r - \epsilon'_{r,L}. \quad (15)$$

This consideration is obsolete for dielectric losses, as losses due to oxygen vacancy formation dominate in CZO, as many times shown in literature.^{33–35,55,56} Therefore, it may be expected that ϵ''_r , shown on the right axis (Figure 5), is generally a function of the p_{O_2} .

Figure 5A,B shows the relative permittivity ϵ'_r and the dielectric loss ϵ''_r for $y = 0.20$ (Ce_{0.80}Zr_{0.20}O₂), respectively, determined from the TM₀₁₀ (≈ 1.18 GHz) and TM₀₂₀ (≈ 2.62 GHz) signal data. Parts (C and D) include the results for $y = 0.33$ (Ce_{0.67}Zr_{0.33}O₂), (E and F) for $y = 0.50$ (Ce_{0.50}Zr_{0.50}O₂), and (G and H) for $y = 0.67$ (Ce_{0.33}Zr_{0.67}O₂). Basically, the powders behave similarly. The dependences on p_{O_2} also agree with the powder data, even independent of mode. The dielectric properties of

all CZO powders are almost constant at low p_{O_2} , with high values for $\Delta\epsilon'_r$ and ϵ''_r . Under these conditions, the inhibition of the hopping mechanism by high oxygen deficiencies δ seems likely.^{21,22,34,43,56} An investigation of the non-stoichiometries in CZO using resonant nanobalance on PLD films (again fabricated from the same material) also supports this hypothesis. The measurements showed that much larger oxygen deficiencies δ exist in CZO compared to CeO₂ at these conditions.^{43,52} At high p_{O_2} , both dielectric properties $\Delta\epsilon'_r$ and ϵ''_r decrease with increasing p_{O_2} , which is typical for CZO at 600°C, as oxygen vacancies are filled up and fewer electrons are available for small polaron hopping.^{33–35}

For a more detailed analysis in this range ($10^{-3} \leq p_{O_2} \leq 0.20$ bar), the $p_{O_2}^m$ -dependence m of CZO powders was determined. The results are shown in Table 3. For Ce_{1-y}Zr_yO_{2- δ} powders with $0.20 \leq y \leq 0.50$ %, similar dependences on the $p_{O_2}^m$ are found in the range $-1/6 < m < -1/4$. Correlations of this magnitude are typical for CZO materials whose properties depend on both intrinsic oxygen vacancies due to chemical reduction (Equation 1, $m = -1/6$) and from extrinsic oxygen vacancies by aliovalent acceptor-type dopants (Equation 3, $m = -1/4$). Corresponding observations were also made at 600°C in one of our previous studies using DC conductivity measurements on sintered CZO ceramics synthesized from the same material.^{43,52} A direct comparison to these results is given in Table 3.

Regarding the $p_{O_2}^m$ -dependence m at high p_{O_2} , a slightly different reaction was observed for Ce_{0.33}Zr_{0.67}O₂, the powder with the highest Zr content (Figure 5G,H). In our

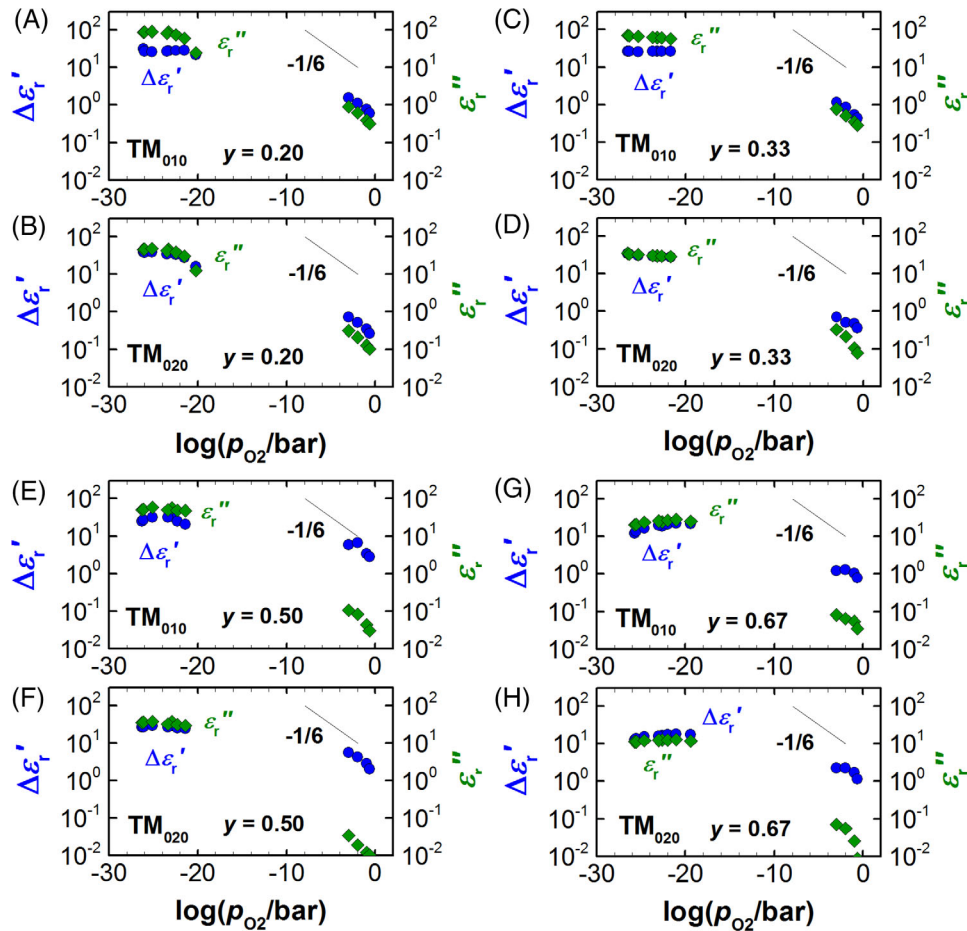


FIGURE 5 Correlation between dielectric parameters (ϵ'_r and ϵ''_r) of CZO and p_{O_2} : results for $Ce_{0.80}Zr_{0.20}O_2$ at (A) TM_{010} (≈ 1.18 GHz) and (B) TM_{020} (≈ 2.62 GHz) modes; analogously (C and D) for $Ce_{0.67}Zr_{0.33}O_2$; (E and F) for $Ce_{0.50}Zr_{0.50}O_2$; (G and H) for $Ce_{0.33}Zr_{0.67}O_2$

TABLE 4 Comparison of $p_{O_2}^m$ -dependences (range: $10^{-3} \leq p_{O_2} \leq 0.20$ bar) of the CZO powders (this RF study, TM_{010} mode, ≈ 1.18 GHz) with sintered CZO ceramics (4-wire measurement, original data from Ref. [43]), made from the same material

Sample	$p_{O_2}^m$ -dependence m	
	Powder	Sintered ceramic ⁴³
$Ce_{0.80}Zr_{0.20}O_2$	-1/5.27	-1/4.48
$Ce_{0.67}Zr_{0.33}O_2$	-1/5.55	-1/4.67
$Ce_{0.50}Zr_{0.50}O_2$	-1/4.31	-1/5.04
$Ce_{0.33}Zr_{0.67}O_2$	-1/7.48	Almost insensitive

previous study the sintered ceramic was almost insensitive to p_{O_2} .⁵² From the microwave data, a small $p_{O_2}^m$ -dependence of $m < 1/7$ (Table 4) can be derived. Studies investigating CZO with $y > 0.50\%$ showed that for high Zr contents the strain in the lattice decreases again and, consequently, the formation of oxygen vacancies is less favored.^{23,34,37} At the same time, ionic conductivity in CZO plays an increasing role at temperatures of 600–800°C. As ionic conductivity is of extrinsic nature (determined by

acceptor-type impurities), it is also not a function of the p_{O_2} . In the case of mixed conductivity (ionic and small polaron), only low $p_{O_2}^m$ -dependences m are expected,^{33,52} as we observed for both the $Ce_{0.33}Zr_{0.67}O_2$ powder and the sintered ceramic (Table 4). Overall, the material behavior under these conditions is typical for CZO and is in good agreement with the literature.^{23,33,34,57,68}

In a next step, the dielectric losses in the CZO powders obtained from the microwave measurements are compared with measurements on sintered ceramics. In the previous study on pure ceria, this comparison in particular has provided clear evidence that the microstructure of CeO_2 has a decisive effect on the defect concentrations and, consequently, on the (di)electrical properties of the material. In order to determine the electrical conductivity of the CZO powders, we first assume, in analogy to Ref. [42], that the polarization losses are negligible compared to the ohmic losses in CZO ($\epsilon''_{Pol} \ll \frac{\sigma}{2\pi f \epsilon_0}$). This assumption allows for a direct determination of the conductivity losses. We will return to why this simplification can be considered legitimate for CZO at a later time.

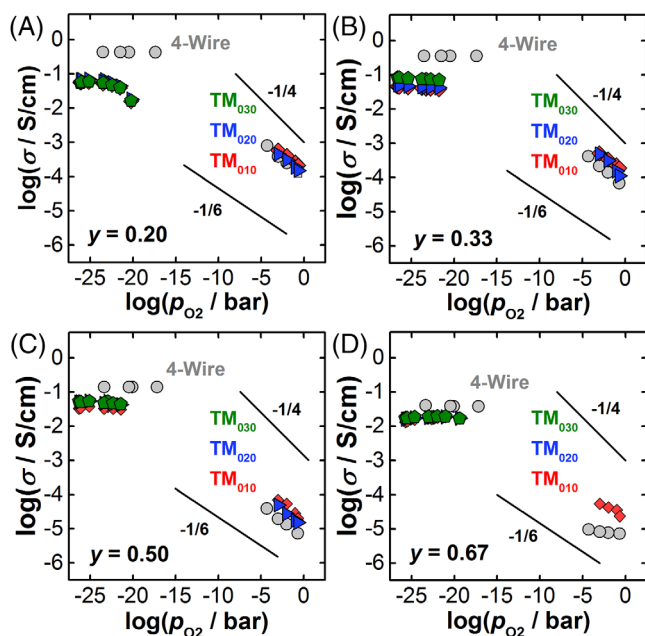


FIGURE 6 Comparison of the conductivities σ of CZO from the microwave measurement with the 4-wire measurement on sintered ceramics (gray, from Ref. [43]) over p_{O_2} at 600°C: (A) $Ce_{0.80}Zr_{0.20}O_2$; (B) $Ce_{0.67}Zr_{0.33}O_2$; (C) $Ce_{0.50}Zr_{0.50}O_2$; (D) $Ce_{0.33}Zr_{0.67}O_2$. TM₀₁₀: red, ≈ 1.18 GHz, TM₀₂₀: blue, ≈ 2.62 GHz, TM₀₃₀: green, ≈ 4.16 GHz

Figure 6 shows the conductivities of CZO calculated from microwave data at 600°C over the p_{O_2} for (A) $Ce_{0.80}Zr_{0.20}O_2$, (B) $Ce_{0.67}Zr_{0.33}O_2$, (C) $Ce_{0.50}Zr_{0.50}O_2$, and (D) $Ce_{0.33}Zr_{0.67}O_2$. The data include the results of TM₀₁₀ (red, ≈ 1.18 GHz) and TM₀₂₀ (blue, ≈ 2.62 GHz) modes. Additionally, the conductivities of their sintered counterpart are plotted for comparison (gray, from Ref. [43]). Due to the lower signal quality of the TM₀₃₀ mode (≈ 4.16 GHz), the data of the TM₀₃₀ mode (green) are only meaningful at large signal amplitudes and are therefore listed exclusively at low p_{O_2} . The same holds for the TM₀₂₀ mode in Figure 6D. For details on resolution limits and details on the corresponding modes, we refer to our previous work^{41,43} in this context.

As the comparison in Figure 6 shows, the losses in the CZO powders are close to findings for the sintered ceramics and the individual modes suggest similar level of conductivity σ . At high p_{O_2} , identical values and $p_{O_2}^m$ -dependencies for the ohmic losses in the CZO are obtained for $0.20 \leq y \leq 0.50$ (Figure 6A–C). The similar properties also suggest that the microstructure only plays a minor role in CZO. These observations are also consistent with findings from comparable studies by other research groups.^{19,20,33,35} Only at a Zr content of $y = 0.67$, higher losses are observed for the powder than for the sintered ceramic (Figure 6D). The higher $p_{O_2}^m$ -dependence (Table 4) suggests that significantly more oxygen vacancies exist in

the powder. The sintered ceramic, on the other hand, is likely to be primarily affected by ionic conductivity.

Now focusing on low p_{O_2} , both samples (powder and sintered ceramic) are insensitive to the p_{O_2} due to the inhibition of small-polaron hopping caused by large non-stoichiometries δ in CZO.^{21,23} However, generally lower losses for the powders are observed than for the sintered ceramics. Based on the defect chemistry model for CZO, there is no plausible explanation why a CZO powder should have lower vacancy concentrations than a sintered ceramic of the same material under the same conditions. Instead, we assume that this effect is due to measurement restrictions of the microwave method itself. Due to the high conductivity in CZO at low p_{O_2} , the penetration depth of the electromagnetic microwaves decreases drastically and an additional weakening of the electric field within the sample is likely. An estimation of the propagation of electromagnetic waves in the GHz range suggests that the penetration depth for permittivities and electrical conductivities typical for CZO under reducing conditions drop to the mm range (note: sample diameter 10 mm). Although the exact dimension of this effect is unclear and is also beyond the scope of our study, a weakening of the electric field nevertheless seems likely. Such an effect would lead to lower signal amplitudes. The real losses occurring in the samples would therefore be larger than determined by the microwave measurement. One indicator of this effect is even provided by measurement: The conductivities of CZO under reducing conditions decrease slightly with the zirconium fraction y (Figure 6), both in the 4-wire and in the microwave measurement. At the same time, the difference between both measurement methods decreases with lower conductivities of the samples. As the field-weakening effect correlates with higher conductivities σ of the sample, this results can be entirely expected in the experiment.

To conclude this section, we will now return to the question of whether polarization losses ϵ''_{Pol} in CZO can indeed be neglected ($\epsilon''_{Pol} \ll \frac{\sigma}{2\pi f \epsilon_0}$). Similar to the study on pure ceria, several indications can be found in the data, which justify the assumption: (1) Studies on conductivities and their dependences for the CZO powders (Figures 5 and 6) showed good agreement with sintered samples of the same material^{43,52} and also with literature from other groups.^{21,23,33,68} If there are other losses in CZO besides conductivity σ , the measured losses in the microwave measurement should have been higher (and possibly even show other dependences). (2) In a multimodal microwave analysis, the measured losses decrease with the higher modes for CZO, which is pictured in Figure 7 for the $Ce_{0.80}Zr_{0.20}O_2$ powder. For this purpose, the data at low p_{O_2} were used, as here the intrinsic small polaron hopping induced by vacancy formation is the

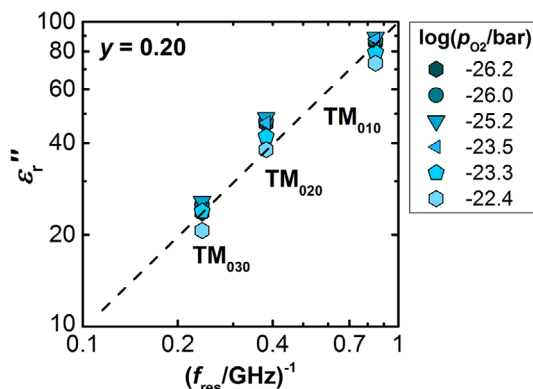


FIGURE 7 Correlation of the dielectric losses ϵ_r'' of $\text{Ce}_{0.80}\text{Zr}_{0.20}\text{O}_2$ and the inverse microwave frequency at low oxygen partial pressures p_{O_2}

dominant conductivity mechanism. The presented data include the information of all three recorded TM modes. The figure indicates a proportional correlation between the measured dielectric losses ϵ_r'' and the inverse microwave frequency (f)⁻¹. Considering Equation (5), this result is a clear indicator that the losses in CZO originate primarily from the conductivity σ , that is, small-polaron hopping. Conversely, this also confirms that polarization losses hardly play a role in CZO and consistently justifies the former assumption. Although small polaron hopping is generally accepted for CZO, the confirmation of the CZO defect model using microwaves (GHz range) is a new approach that has not been presented before.

Overall, the results are consistent with literature and are in-line with our earlier microwave investigations.⁴² The derived defect mechanisms are also in good agreement with the current understanding of the CZO defect chemistry.

3.3 | Impact of Zr on defect chemistry of CZO

In this chapter, the effect of the Zr content y on the electrical conductivity of the CZO powders is analyzed in this section, and compared with the data from pure ceria.⁴² Figure 8 shows the electrical conductivity of the CZO powders with the Zr content at 600°C (A) at high p_{O_2} (10^{-3} bar) and (B) at low p_{O_2} (10^{-23} bar). As shown in (A), the conductivity of CZO increases initially at oxidizing conditions due to the strain in the crystal ($0.20 \leq y \leq 0.33$) but decreases noticeably at higher y . Similar correlations are observed for reducing conditions (B). The microwave results for CZO therefore suggest that the incorporation of Zr^{4+} into the lattice leads to a higher concentration of

oxygen vacancies and increases the practically achievable oxygen non-stoichiometry δ in CZO, as long as the Zr content is not too large. The fundamental findings agree with results documented for sintered ceramics and PLD coatings (the same material).^{43,52} The effect can be explained by the so-called size effect. Thereby, the small Zr^{4+} cations energetically favor the formation of oxygen vacancies at Ce-lattice sites.^{58–60}

Furthermore, the conductivity of CeO_2 compared to CZO at high p_{O_2} (A) differs from those at reducing conditions (B). Although the ceria powder shows similar conductivities as CZO ($y = 0.20, \dots, 0.33$) at high p_{O_2} , the conductivity is significantly lower compared to CZO at low p_{O_2} . The reason for this effect is assigned to the effect of microstructure on the nanocrystalline CeO_2 sample. Therefore, at high p_{O_2} , the ceria properties are affected by the energetically favored reduction of the near-surface regions and cause similar conductivities like in CZO.^{19,69,70} This hypothesis was also confirmed by the low activation energy for the defect formation of the ceria powder sample.⁴² On the other hand, sample morphology becomes less important at low p_{O_2} . As the p_{O_2} decreases, more and more oxygen vacancies are formed in deeper layers of the material. Here, higher oxygen non-stoichiometries δ can be achieved in CZO, which in turn can be attributed to the “size effect” that energetically promotes the release of oxygen near Zr sites.^{58–60} As a consequence, much higher conductivities are observed in CZO (compared to ceria). Due to the assumed field weakening in the measurement (see the previous section), it can also be assumed that the effect in the measurement is rather underestimated and the real effect is probably even larger.

As a last step in our analysis, the effect of Zr on the polarization and therefore on the permittivity of the material will be examined, in particular, how the formation of oxygen vacancies affects the polarization in CZO. Figure 9 shows the change in the relative permittivity $\Delta\epsilon_r'$ by the chemical reduction of CZO at 600°C. The change $\Delta\epsilon_r'$ is referenced to the polarization properties of CZO at reducing ($p_{\text{O}_2} = 10^{-23}$ bar) and oxidizing conditions ($p_{\text{O}_2} = 0.21$ bar) (similar to Equation 13).

The increase in polarization due to reduction in ceria is much weaker compared to CZO. A maximum can be observed at $y \leq 0.20$, with a slightly decreasing tendency at higher Zr fractions. The observation correlates with the results on CZO conductivity (Figure 8B). Therefore, the data suggest that the increasing polarization is directly associated with the formation of oxygen vacancies in CZO. A comparison with the values for ϵ_r' at room temperature (Table 3) shows that the increase in relative permittivity $\Delta\epsilon_r'$ due to vacancy formation is similar in magnitude to the polarization in the lattice in stoichiometric CZO. Oxygen non-stoichiometry therefore leads to approximately a

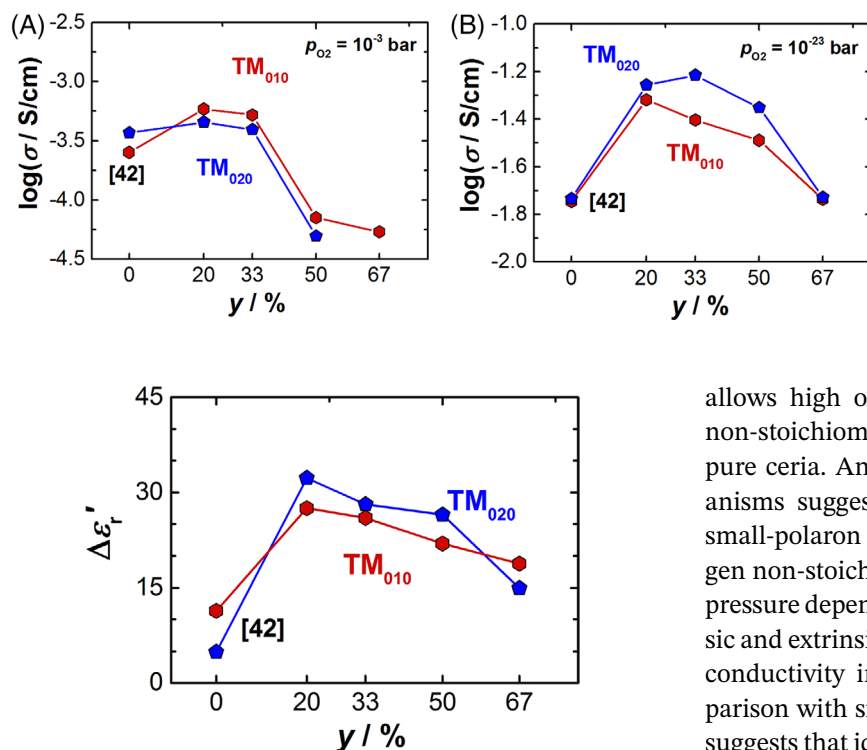


FIGURE 8 Effect of Zr concentration y on the electrical conductivity σ of $Ce_{1-y}Zr_yO_{2-\delta}$ powders at $600^\circ C$: (A) high p_{O_2} (10^{-3} bar); (B) low p_{O_2} (10^{-23} bar)

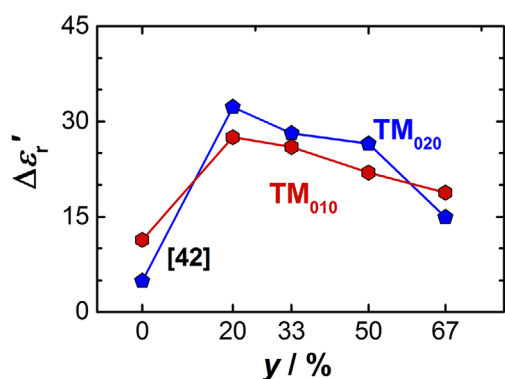


FIGURE 9 Effect of Zr concentration y on the change of relative permittivity $\Delta\epsilon_r'$ of the $Ce_{1-y}Zr_yO_{2-\delta}$ powders (between $p_{O_2} = 10^{-23}$ bar and $p_{O_2} = 0.21$ bar) at $600^\circ C$

doubling of the total relative permittivity in CZO, with the highest effect for $Ce_{0.80}Zr_{0.20}O_2$. The higher relative permittivity ϵ_r' in reduced ceria and CZO was also reported in other studies.^{103,106} Nevertheless, the question remains what kind of mechanism causes the increase in polarization. We have already made some proposals for this in our previous publication.⁴² The reduction of CZO (according to Equation 1) leads to the formation of oxygen vacancies in the lattice with two reduced Ce^{3+} cations with additional electrons e^- . The result is a (twofold) positively charged (empty) oxygen site and a negatively charged Ce site (compared to the original configuration in the lattice), which might induce an additional dipole moment.

4 | CONCLUSIONS

In the present study, the dielectric properties of CZO were investigated by the MCP method. Ceria–zirconia solid solution powders with a wide range of compositions ($y = 0.2, 0.33, 0.50,$ and 0.67) were subject of the study. The effect of temperature on the reducibility of CZO was analyzed in a first step. Here, Zr in ceria was found to inhibit the kinetics of oxygen exchange at low temperatures. Experiments related to dielectric losses at $600^\circ C$ and a large p_{O_2} -range confirmed that CZO

allows high oxygen vacancy concentrations (or oxygen non-stoichiometries δ) at low p_{O_2} , especially compared to pure ceria. An analysis of the fundamental defect mechanisms suggests that at low p_{O_2} , the inhibition of the small-polaron mechanism also occurs due to high oxygen non-stoichiometries.^{21,33,57} Instead, the oxygen partial pressure dependencies at high p_{O_2} suggest that both intrinsic and extrinsic oxygen vacancies contribute to the overall conductivity in CZO under these conditions. The comparison with sintered ceramics^{43,52} (of the same material) suggests that identical mechanisms dominate in both sample sets and, unlike CeO_2 ,⁴² microstructure plays only a minor role in CZO. Moreover, for the first time, we used a multimodal microwave approach and found evidence that the conductivity in the material is indeed of electronic origin (small polarons). On the other hand, polarization losses in the CZO are not significant. Furthermore, the chemical reduction of CZO was observed to be accompanied by a stronger permittivity, which correlates with the concentration of oxygen vacancies in CZO. Thus, our study is one of the few to use microwaves to characterize CZO powder samples and provides a comprehensive data set for the dielectric properties of CZO that has not been shown before. The results are consistent with the understanding of the CZO defect chemistry and are in good agreement with findings from our previous fundamental- and application-oriented studies.^{41–44,50,52} The data set about the correlation between defect chemistry and the dielectric properties of CZO can also provide valuable information for the microwave-assisted diagnosis of CZO-based oxygen storage and electrolyte materials.

ACKNOWLEDGMENTS

This research was funded by the Deutsche Forschungsgemeinschaft (DFG), DFG Grants MO 1060/29-1 and FR 1301/23-1. The authors are indebted to Mrs. Mergner for the preparation of the SEM samples, Mrs. Haider (Bayreuth Institute of Macromolecular Research) for SEM imaging, Mrs. Jena (Chair of Applied Mechanics and Fluid Dynamics, Prof. Sesterhenn) for particle size measurements, and the Department of Metals and Alloys (Prof. Uwe Glatzel) for XRD measurements.

Open access funding enabled and organized by Projekt DEAL.

CONFLICTS OF INTEREST

The authors declare no conflicts of interest.

ORCID

Carsten Steiner  <https://orcid.org/0000-0002-1410-6979>

Ralf Moos  <https://orcid.org/0000-0001-7622-0120>

REFERENCES

- Larimi AS, Alavi SM. Ceria-zirconia supported Ni catalysts for partial oxidation of methane to synthesis gas. *Fuel*. 2012;102:366–71. <https://doi.org/10.1016/j.fuel.2012.06.050>
- Abanades S, Legal A, Cordier A, Peraudeau G, Flamant G, Julbe A. Investigation of reactive cerium-based oxides for H₂ production by thermochemical two-step water-splitting. *J Mat Sci*. 2010;45(15):4163–73. <https://doi.org/10.1007/s10853-010-4506-4>
- Luciani G, Landi G, Di Benedetto A. Syngas production through H₂O/CO₂ thermochemical splitting over doped ceria-zirconia materials. *Front Energy Res*. 2020;8:180. <https://doi.org/10.3389/fenrg.2020.00204>
- Wang Q, Zhao B, Li G, Zhou R. Application of rare earth modified Zr-based ceria-zirconia solid solution in three-way catalyst for automotive emission control. *Environ Sci Technol*. 2010;44(10):3870–5. <https://doi.org/10.1021/es903957e>
- Trovarelli A. Catalytic properties of ceria and CeO₂-containing materials. *Catal Rev: Sci Eng*. 1996;38(4):439–520. <https://doi.org/10.1080/01614949608006464>
- Mußmann L, Lindner D, Lox ES, van Yperen R, Kreuzer TP, Mitsushima I, et al. The role of zirconium in novel three-way catalysts. *SAE Trans*. 1997;106(4):136–47. <https://doi.org/10.4271/970465>
- Montini T, Melchionna M, Monai M, Fornasiero P. Fundamentals and catalytic applications of CeO₂-based materials. *Chem Rev*. 2016;116(10):5987–6041. <https://doi.org/10.1021/acs.chemrev.5b00603>
- Orihuela MP, Miceli P, Ramírez-Rico J, Fino D, Chacartegui R. Ceria-based catalytic coatings on biomorphic silicon carbide: a system for soot oxidation with enhanced properties. *Chem Eng J*. 2021;415(1–3):128959. <https://doi.org/10.1016/j.cej.2021.128959>
- Czerwinski F, Szpunar JA. The nanocrystalline ceria sol-gel coatings for high temperature applications. *J Sol-Gel Sci Technol*. 1997;9(1):103–14. <https://doi.org/10.1007/BF02439341>
- Murray EP, Tsai T, Barnett SA. A direct-methane fuel cell with a ceria-based anode. *Nature*. 1999;400(6745):649–51. <https://doi.org/10.1038/23220>
- Chueh WC, Hao Y, Jung W, Haile SM. High electrochemical activity of the oxide phase in model ceria-Pt and ceria-Ni composite anodes. *Nat Mater*. 2011;11(2):155–61. <https://doi.org/10.1038/nmat3184>
- Ling Y, Wang X, Ma Z, Wei K, Wu Y, Khan M, et al. Review of experimental and modelling developments for ceria-based solid oxide fuel cells free from internal short circuits. *J Mat Sci*. 2020;55(1):1–23. <https://doi.org/10.1007/s10853-019-03876-z>
- Fergus JW. Electrolytes for solid oxide fuel cells. *J Power Sources*. 2006;162(1):30–40. <https://doi.org/10.1016/j.jpowsour.2006.06.062>
- Rojek-Wöckner VA, Opitz AK, Brandner M, Mathé J, Bram M. A novel Ni/ceria-based anode for metal-supported solid oxide fuel cells. *J Power Sources*. 2016;328(1):65–74. <https://doi.org/10.1016/j.jpowsour.2016.07.075>
- Khan SB, Akhtar K, editors. Introductory chapter: cerium oxide – applications and attributes. In: *Cerium oxide – applications and attributes*. London: IntechOpen; 2019.
- Dezfuli AS, Ganjali MR, Naderi HR, Norouzi P. A high performance supercapacitor based on a ceria/graphene nanocomposite synthesized by a facile sonochemical method. *RSC Adv*. 2015;5(57):46050–8. <https://doi.org/10.1039/C5RA02957K>
- Ghosh S, Anbalagan K, Kumar UN, Thomas T, Rao GR. Ceria for supercapacitors: dopant prediction, and validation in a device. *Appl Mater Today*. 2020;21:100872. <https://doi.org/10.1016/j.apmt.2020.100872>
- Tuller HL, Nowick AS. Small polaron electron transport in reduced CeO₂ single crystals. *J Phys Chem Solids*. 1977;38(8):859–67. [https://doi.org/10.1016/0022-3697\(77\)90124-X](https://doi.org/10.1016/0022-3697(77)90124-X)
- Chiang Y-M, Lavik EB, Kosacki I, Tuller HL, Ying JY. Defect and transport properties of nanocrystalline CeO_{2-x}. *Appl Phys Lett*. 1996;69(2):185–7. <https://doi.org/10.1063/1.117366>
- Chiang Y-M, Lavik EB, Kosacki I, Tuller HL, Ying JY. Non-stoichiometry and electrical conductivity of nanocrystalline CeO_{2-x}. *J Electroceram*. 1997;1(1):7–14. <https://doi.org/10.1023/A:1009934829870>
- Chen Di, Y Cao, Weng D, Tuller HL. Defect and transport model of ceria-zirconia solid solutions: Ce_{0.8}Zr_{0.2}O_{2-δ}—an electrical conductivity study. *Chem Mater*. 2014;26(17):5143–50. <https://doi.org/10.1021/cm502565b>
- Hao Y, Yang C-K, Haile SM. Ceria-zirconia solid solutions (Ce_{1-x}Zr_xO_{2-δ}; x ≤ 0.2) for solar thermochemical water splitting: a thermodynamic study. *Chem Mater*. 2014;26(20):6073–82. <https://doi.org/10.1021/cm503131p>
- Kuhn M, Bishop SR, Rupp JLM, Tuller HL. Structural characterization and oxygen nonstoichiometry of ceria-zirconia (Ce_{1-x}Zr_xO_{2-δ}) solid solutions. *Acta Mater*. 2013;61(11):4277–88. <https://doi.org/10.1016/j.actamat.2013.04.001>
- Giuliano M, Ricchiardi G, Damin A, Sgroi M, Nicol G, Parussa F. Thermal ageing effects in a commercial three-way catalyst: physical characterization of washcoat and active metal evolution. *Int J Automot Technol*. 2020;21(2):329–37. <https://doi.org/10.1007/s12239-020-0031-x>
- Rood S, Eslava S, Manigrasso A, Bannister C. Recent advances in gasoline three-way catalyst formulation: a review. *Proc Inst Mech Eng, D*. 2020;234(4):936–49. <https://doi.org/10.1177/0954407019859822>
- Jiang JC, Pan XQ, Graham GW, McCabe RW, Schwank J. Microstructure of a Pd/ceria-zirconia catalyst after high-temperature aging. *Catal Lett*. 1998;53(1/2):37–42. <https://doi.org/10.1023/A:1019089318822>
- Ozawa M, Okouchi T, Haneda M. Three way catalytic activity of thermally degenerated Pt/Al₂O₃ and Pt/CeO₂-ZrO₂ modified Al₂O₃ model catalysts. *Catal Today*. 2015;242:329–37. <https://doi.org/10.1016/j.cattod.2014.06.013>
- Hou X, Zhao K, Marina OA, Grant Norton M, Ha S. NiMo-ceria-zirconia-based anode for solid oxide fuel cells operating on gasoline surrogate. *Appl Catal B*. 2019;242:31–9. <https://doi.org/10.1016/j.apcatb.2018.09.095>

29. Omar S. Doped ceria for solid oxide fuel cells. In: Khan SB, Akhtar K, editors. Cerium oxide – applications and attributes. London: IntechOpen; 2019.
30. Tompsett GA, Sammes NM, Yamamoto O. Ceria-yttria-stabilized zirconia composite ceramic systems for applications as low-temperature electrolytes. *J Am Ceram Soc.* 1997;80(12):3181–6. <https://doi.org/10.1111/j.1151-2916.1997.tb03247.x>
31. Artini C, Carnasciali MM, Viviani M, Presto S, Plaisier JR, Costa GA, et al. Structural properties of Sm-doped ceria electrolytes at the fuel cell operating temperatures. *Solid State Ionics.* 2018;315:85–91. <https://doi.org/10.1016/j.ssi.2017.12.009>
32. Jung W, Dereux JO, Chueh WC, Hao Y, Haile SM. High electrode activity of nanostructured, columnar ceria films for solid oxide fuel cells. *Energy Environ Sci.* 2012;5(9):8682. <https://doi.org/10.1039/c2ee22151a>
33. Lee J-H, Yoon SM, Kim B-K, Lee H-W, Song HS. Electrical conductivity and defect structure of CeO₂-ZrO₂ mixed oxide. *J Mat Sci.* 2002;37(6):1165–71. <https://doi.org/10.1023/A:1014363304942>
34. Boaro M. Electrical and oxygen storage/release properties of nanocrystalline ceria zirconia solid solutions. *Solid State Ionics.* 2002;147(1–2):85–95. [https://doi.org/10.1016/S0167-2738\(02\)00004-8](https://doi.org/10.1016/S0167-2738(02)00004-8)
35. Kim T, Vohs JM, Gorte RJ. Thermodynamic investigation of the redox properties of ceria–zirconia solid solutions. *Ind Eng Chem Res.* 2006;45(16):5561–5. <https://doi.org/10.1021/ie0511478>
36. Chen H-T, Chang J-G. Oxygen vacancy formation and migration in Ce_{1-x}Zr_xO₂ catalyst: a DFT+ U calculation. *J Phys Chem.* 2010;132(21):214702. <https://doi.org/10.1063/1.3429314>
37. Balducci G, Kašpar J, Fornasiero P, Graziani M, Islam MS, Gale JD. Computer simulation studies of bulk reduction and oxygen migration in CeO₂-ZrO₂ solid solutions. *J Phys Chem B.* 1997;101(10):1750–3. <https://doi.org/10.1021/jp962530g>
38. Dietrich M, Rauch D, Porch A, Moos R. A laboratory test setup for in situ measurements of the dielectric properties of catalyst powder samples under reaction conditions by microwave cavity perturbation: set up and initial tests. *Sensors.* 2014;14(9):16856–68. <https://doi.org/10.3390/s140916856>
39. Pozar DM. Microwave engineering. 4th ed. Hoboken, NJ, USA: John Wiley & Sons; 2012.
40. Chen LF, Ong CK, Neo CP, Varadan VV, Varadan VK. Microwave electronics – measurement and materials characterization. Hoboken, NJ, USA: John Wiley & Sons; 2004.
41. Steiner C, Walter S, Malashchuk V, Hagen G, Kogut I, Fritze H, et al. Determination of the dielectric properties of storage materials for exhaust gas aftertreatment using the microwave cavity perturbation method. *Sensors.* 2020;20(21):6024. <https://doi.org/10.3390/s20216024>
42. Steiner C, Hagen G, Kogut I, Fritze H, Moos R. Analysis of defect chemistry and microstructural effects of non-stoichiometric ceria by the high-temperature microwave cavity perturbation method. *J Eur Ceram Soc.* 2022;42(2):499–511. <https://doi.org/10.1016/j.jeurceramsoc.2021.08.053>
43. Kogut I, Steiner C, Wulfmeier H, Wollbrink A, Hagen G, Moos R, et al. Comparison of the electrical conductivity of bulk and film Ce_{1-x}Zr_xO_{2-δ} in oxygen-depleted atmospheres at high temperatures. *J Mat Sci.* 2021;56:17191–204. <https://doi.org/10.1007/s10853-021-06348-5>
44. Steiner C, Gänzler AM, Zehentbauer M, Hagen G, Casapu M, Müller S, et al. Oxidation state and dielectric properties of ceria-based catalysts by complementary microwave cavity perturbation and X-ray absorption spectroscopy measurements. *Top Catal.* 2019;62(1–4):227–36. <https://doi.org/10.1007/s11244-018-1110-3>
45. Moos R, Wedemann M, Spörl M, Reiß S, Fischerauer G. Direct catalyst monitoring by electrical means: an overview on promising novel principles. *Top Catal.* 2009;52(13–20):2035–40. <https://doi.org/10.1007/s11244-009-9399-6>
46. Müller SA, Degler D, Feldmann C, Türk M, Moos R, Fink K, et al. Exploiting synergies in catalysis and gas sensing using noble metal-loaded oxide composites. *ChemCatChem.* 2018;10(5):864–80. <https://doi.org/10.1002/cctc.201701545>
47. Beulertz G, Votsmeier M, Moos R. Effect of propene, propane, and methane on conversion and oxidation state of three-way catalysts: a microwave cavity perturbation study. *Appl Catal B.* 2015;165:369–77. <https://doi.org/10.1016/j.apcatb.2014.09.068>
48. Beulertz G, Votsmeier M, Moos R. In operando detection of three-way catalyst aging by a microwave-based method: initial studies. *Appl Sci.* 2015;5(3):174–86. <https://doi.org/10.3390/app5030174>
49. Reiß S, Wedemann M, Spörl M, Fischerauer G, Moos R. Effects of H₂O, CO₂, CO, and flow rates on the RF-based monitoring of three-way catalysts. *Sens Lett.* 2011;9(1):316–20. <https://doi.org/10.1166/sl.2011.1472>
50. Steiner C, Malashchuk V, Kubinski D, Hagen G, Moos R. Catalyst state diagnosis of three-way catalytic converters using different resonance parameters—a microwave cavity perturbation study. *Sensors.* 2019;19(16):3559. <https://doi.org/10.3390/s19163559>
51. Moos R, Spörl M, Hagen G, Gollwitzer A, Wedemann M, Fischerauer G. TWC: lambda control and OBD without lambda probe – an initial approach. *SAE Tech Pap.* 2008-01-0916 (2008). <https://doi.org/10.4271/2008-01-0916>
52. Kogut I, Wollbrink A, Steiner C, Wulfmeier H, El Azzouzi F-E, Moos R, et al. Linking the electrical conductivity and non-stoichiometry of thin film Ce_{1-x}Zr_xO_{2-δ} by a resonant nanobalance approach. *Materials.* 2021;14(4):748. <https://doi.org/10.3390/ma14040748>
53. Eguchi K, Setoguchi T, Inoue T, Arai H. Electrical properties of ceria-based oxides and their application to solid oxide fuel cells. *Solid State Ionics.* 1992;52(1–3):165–72. [https://doi.org/10.1016/0167-2738\(92\)90102-U](https://doi.org/10.1016/0167-2738(92)90102-U)
54. Schneider D, Gödickemeier M, Gauckler LJ. Nonstoichiometry and defect chemistry of ceria solid solutions. *J Electroceram.* 1997;1(2):165–72. <https://doi.org/10.1023/A:1009928817542>
55. Xiong Y-P, Kishimoto H, Yamaji K, Yoshinaga M, Horita T, Brito ME, et al. Electronic conductivity of pure ceria. *Solid State Ionics.* 2011;192(1):476–9. <https://doi.org/10.1016/j.ssi.2010.07.017>
56. Tuller HL, Nowick AS. Defect structure and electrical properties of nonstoichiometric CeO₂ single crystals. *J Electrochem Soc.* 1979;126(2):209–17. <https://doi.org/10.1149/1.2129007>
57. Schmitt R, Nenning A, Kraynis O, Korobko R, Frenkel AI, Lubomirsky I, et al. A review of defect structure and chemistry

- in ceria and its solid solutions. *Chem Soc Rev.* 2020;49(2):554–92. <https://doi.org/10.1039/C9CS00588A>
58. Yang Z, Woo TK, Hermansson K. Effects of Zr doping on stoichiometric and reduced ceria: a first-principles study. *J Chem Phys.* 2006;124(22):224704. <https://doi.org/10.1063/1.2200354>
 59. Dutta G, Waghmare UV, Baidya T, Hegde MS, Priolkar KR, Sarode PR. Reducibility of $Ce_{1-x}Zr_xO_2$: origin of enhanced oxygen storage capacity. *Catal Lett.* 2006;108(3–4):165–72. <https://doi.org/10.1007/s10562-006-0040-z>
 60. Wang H-F, Guo Y-L, Lu G-Z, Hu P. Maximizing the localized relaxation: the origin of the outstanding oxygen storage capacity of κ - $Ce_2Zr_2O_8$. *Angew Chem Int Ed Engl.* 2009;48(44):8289–92. <https://doi.org/10.1002/anie.200903907>
 61. Keating PRL, Scanlon DO, Morgan BJ, Galea NM, Watson GW. Analysis of intrinsic defects in CeO_2 using a Koopmans-like GGA+ U approach. *J Phys Chem C.* 2012;116(3):2443–52. <https://doi.org/10.1021/jp2080034>
 62. Gopal CB, van de Walle A. *Ab initio* thermodynamics of intrinsic oxygen vacancies in ceria. *Phys Rev B.* 2012;86(13). <https://doi.org/10.1103/PhysRevB.86.134117>
 63. Murgida GE, Ferrari V, Ganduglia-Pirovano MV, Llois AM. Ordering of oxygen vacancies and excess charge localization in bulk ceria: a DFT+ U study. *Phys Rev B.* 2014;90(11). <https://doi.org/10.1103/PhysRevB.90.115120>
 64. Han X, Amrane N, Zhang Z, Benkraouda M. Oxygen vacancy ordering and electron localization in CeO_2 : hybrid functional study. *J Phys Chem C.* 2016;120(25):13325–31. <https://doi.org/10.1021/acs.jpcc.6b00865>
 65. Zacherle T, Schriever A, de Souza RA, Martin M. *Ab initio* analysis of the defect structure of ceria. *Phys Rev B.* 2013;87(13):55. <https://doi.org/10.1103/PhysRevB.87.134104>
 66. Panlener RJ, Blumenthal RN, Garnier JE. A thermodynamic study of nonstoichiometric cerium dioxide. *J Phys Chem Solids.* 1975;36(11):1213–22. [https://doi.org/10.1016/0022-3697\(75\)90192-4](https://doi.org/10.1016/0022-3697(75)90192-4)
 67. Duncan KL, Wang Y, Bishop SR, Ebrahimi F, Wachsman ED. The role of point defects in the physical properties of nonstoichiometric ceria. *J Appl Phys.* 2007;101(4):44906. <https://doi.org/10.1063/1.2559601>
 68. Rupp J, Gauckler L. Microstructures and electrical conductivity of nanocrystalline ceria-based thin films. *Solid State Ionics.* 2006;177(26–32):2513–8. <https://doi.org/10.1016/j.ssi.2006.07.033>
 69. Kim S, Maier J. On the conductivity mechanism of nanocrystalline ceria. *J Electrochem Soc.* 2002;149(10):J73. <https://doi.org/10.1149/1.1507597>
 70. Suzuki T, Kosacki I, Anderson HU, Colomban P. Electrical conductivity and lattice defects in nanocrystalline cerium oxide thin films. *J Am Ceram Soc.* 2001;84(9):2007–14. <https://doi.org/10.1111/j.1151-2916.2001.tb00950.x>
 71. Tschöpe A. Grain size-dependent electrical conductivity of polycrystalline cerium oxide II: space charge model. *Solid State Ionics.* 2001;139(3–4):267–80. [https://doi.org/10.1016/S0167-2738\(01\)00677-4](https://doi.org/10.1016/S0167-2738(01)00677-4)
 72. Tschöpe A. Space charge layers in polycrystalline cerium oxide. *MRS Proc.* 2002;756:190. <https://doi.org/10.1557/PROC-756-EE4.2>
 73. Kim S, Fleig J, Maier J. Space charge conduction: simple analytical solutions for ionic and mixed conductors and application to nanocrystalline ceria. *Phys Chem Chem Phys.* 2003;5(11):2268–73. <https://doi.org/10.1039/B300170A>
 74. Zurhelle AF, Tong X, Klein A, Mebane DS, de Souza RA. A space-charge treatment of the increased concentration of reactive species at the surface of a ceria solid solution. *Angew Chem Int Ed Engl.* 2017;56(46):14516–20. <https://doi.org/10.1002/anie.201708118>
 75. Göbel MC, Gregori G, Guo X, Maier J. Boundary effects on the electrical conductivity of pure and doped cerium oxide thin films. *Phys Chem Chem Phys.* 2010;12(42):14351–61. <https://doi.org/10.1039/C0CP00385A>
 76. Göbel MC, Gregori G, Maier J. Size effects on the electrical conductivity of ceria: achieving low space charge potentials in nanocrystalline thin films. *J Phys Chem C.* 2013;117(44):22560–8. <https://doi.org/10.1021/jp407585w>
 77. Lamas DG, Fuentes RO, Fábregas IO, Fernández de Rapp ME, Lascalea GE, Casanova JR, et al. Synchrotron X-ray diffraction study of the tetragonal–cubic phase boundary of nanocrystalline ZrO_2 – CeO_2 synthesized by a gel-combustion process. *J Appl Crystallogr.* 2005;38(6):867–73. <https://doi.org/10.1107/S0021889805025343>
 78. Jimenez R, Bucheli W, Varez A, Sanz J. Humidity related low temperature conductivity hysteresis of $Ce_{1-x}Zr_xO_2$ ($0 \leq x \leq 1$) ceramics. Structural disorder relationship. *Fuel Cells.* 2011;11(5):642–53. <https://doi.org/10.1002/fuce.201000185>
 79. Yashima M, Arashi H, Kakihana M, Yoshimura M. Raman scattering study of cubic-tetragonal phase transition in $Zr_{1-x}Ce_xO_2$ solid solution. *J Am Ceram Soc.* 1994;77(4):1067–71. <https://doi.org/10.1111/j.1151-2916.1994.tb07270.x>
 80. Yashima M, Sasaki S, Yamaguchi Y, Kakihana M, Yoshimura M, Mori T. Internal distortion in ZrO_2 – CeO_2 solid solutions: neutron and high-resolution synchrotron X-ray diffraction study. *Appl Phys Lett.* 1998;72(2):182–4. <https://doi.org/10.1063/1.120678>
 81. Varez A, Garcia-Gonzalez E, Sanz J. Cation miscibility in CeO_2 – ZrO_2 oxides with fluorite structure. a combined TEM, SAED and XRD Rietveld analysis. *J Mater Chem.* 2006;16(43):4249–56. <https://doi.org/10.1039/B607778A>
 82. Wakita T, Yashima M. In situ observation of the tetragonal-cubic phase transition in the $CeZrO_4$ solid solution – a high-temperature neutron diffraction study. *Acta Crystallogr, Sect B: Struct Sci.* 2007;63(Pt 3):384–9. <https://doi.org/10.1107/S0108768107007720>
 83. Yashima M, Sekikawa T, Sato D, Nakano H, Omoto K. Crystal structure and oxide-ion diffusion of nanocrystalline, compositionally homogeneous ceria–zirconia $Ce_{0.5}Zr_{0.5}O_2$ up to 1176 K. *Cryst Growth Des.* 2013;13(2):829–37. <https://doi.org/10.1021/cg301530t>
 84. Yashima M, Morimoto K, Ishizawa N, Yoshimura M. Zirconia-ceria solid solution synthesis and the temperature-time-transformation diagram for the 1:1 composition. *J Am Ceram Soc.* 1993;76(7):1745–50. <https://doi.org/10.1111/j.1151-2916.1993.tb06643.x>
 85. Varez A, Garcia-Gonzalez E, Jolly J, Sanz J. Structural characterization of $Ce_{1-x}Zr_xO_2$ ($0 \leq x \leq 1$) samples prepared at 1650°C by solid state reaction. *J Eur Ceram Soc.* 2007;27(13–15):3677–82. <https://doi.org/10.1016/j.jeurceramsoc.2007.02.014>
 86. Yashima M, Morimoto K, Ishizawa N, Yoshimura M. Diffusionless tetragonal-cubic transformation temperature in

- zirconia-ceria solid solutions. *J Am Ceram Soc.* 1993;76(11):2865–8. <https://doi.org/10.1111/j.1151-2916.1993.tb04028.x>
87. Chen P, Schönebaum S, Simons T, Rauch D, Dietrich M, Moos R, et al. Correlating the integral sensing properties of zeolites with molecular processes by combining broadband impedance and DRIFT spectroscopy – a new approach for bridging the scales. *Sensors.* 2015;15(11):28915–41. <https://doi.org/10.3390/s151128915>
 88. Lin M, Afsar M. A new cavity perturbation technique for accurate measurement of dielectric parameters. In: *IEEE MTT-S Int Microw Symp Dig.* 2006. p. 1630–3. <https://doi.org/10.1109/MWSYM.2006.249650>
 89. Moos R, Beulertz G, Reiß S, Hagen G, Fischerauer G, Votsmeier M, et al. Overview: status of the microwave-based automotive catalyst state diagnosis. *Top Catal.* 2013;56(1–8):358–64. <https://doi.org/10.1007/s11244-013-9980-x>
 90. Parkash A, Vaid JK, Mansingh A. Measurement of dielectric parameters at microwave frequencies by cavity-perturbation technique. *IEEE Trans Microwave Theory Tech.* 1979;27(9):791–5. <https://doi.org/10.1109/TMTT.1979.1129731>
 91. Leong K, Mazierska J. Precise measurements of the *Q* factor of dielectric resonators in the transmission mode—accounting for noise, crosstalk, delay of uncalibrated lines, coupling loss, and coupling reactance. *IEEE Trans Microwave Theory Tech.* 2002;50(9):2115–27. <https://doi.org/10.1109/TMTT.2002.802324>
 92. Waldron RA. Perturbation theory of resonant cavities. *Proc IEE, C Monographs.* 1960;107(12):272. <https://doi.org/10.1049/pi-c.1960.0041>
 93. Inoue R, Miwa K, Kitano H, Maeda A, Odate Y, Tanabe E. Highly accurate and real-time determination of resonant characteristics: complex linear regression of the transmission coefficient. *IEEE Trans Microwave Theory Tech.* 2004;52(9):2163–8. <https://doi.org/10.1109/TMTT.2004.834183>
 94. Bozorth RM, Chapin DM. Demagnetizing factors of rods. *J Appl Phys.* 1942;13(5):320–6. <https://doi.org/10.1063/1.1714873>
 95. Cuenca JA, Klein S, Ruger R, Porch A. Microwave complex permeability of magnetite using non-demagnetising and demagnetising cavity modes. In: *Eur Microwave Conf (EuMC).* 2014:128–31. <https://doi.org/10.1109/EuMC.2014.6986386>
 96. Kobayashi H, Ogawa S. Dielectric constant and conductivity measurement of powder samples by the cavity perturbation method. *Jpn J Appl Phys.* 1971;10(3):345–50. <https://doi.org/10.1143/JJAP.10.345>
 97. Farra R, García-Melchor M, Eichelbaum M, Hashagen M, Frandsen W, Allan J, et al. Promoted ceria: a structural, catalytic, and computational study. *ACS Catal.* 2013;3(10):2256–68. <https://doi.org/10.1021/cs4005002>
 98. Dube DC. Study of Landau-Lifshitz-Looyenga's formula for dielectric correlation between powder and bulk. *J Phys D: Appl Phys.* 1970;3(11):1648–52. <https://doi.org/10.1088/0022-3727/3/11/313>
 99. Looyenga H. Dielectric constants of heterogeneous mixtures. *Physica.* 1965;31(3):401–6. [https://doi.org/10.1016/0031-8914\(65\)90045-5](https://doi.org/10.1016/0031-8914(65)90045-5)
 100. Marquardt P. Quantum-size affected conductivity of mesoscopic metal particles. *Phys Lett A.* 1987;123(7):365–8. [https://doi.org/10.1016/0375-9601\(87\)90396-3](https://doi.org/10.1016/0375-9601(87)90396-3)
 101. Marquardt P, Nimtz G. Size-governed electromagnetic absorption by metal particles. *Phys Rev B Condens Matter Mater Phys.* 1989;40(11):7996–8. <https://doi.org/10.1103/PhysRevB.40.7996>
 102. Schulz M, Fritze H, Stenzel C. Measurement and control of oxygen partial pressure at elevated temperatures. *Sens Actuators B Chem.* 2013;187:503–8. <https://doi.org/10.1016/j.snb.2013.02.115>
 103. Dutta G, Saha SK, Waghmare UV. Effects of Zr and Ti doping on the dielectric response of CeO₂: a comparative first-principles study. *Solid State Commun.* 2010;150(41–42):2020–2. <https://doi.org/10.1016/j.ssc.2010.08.014>
 104. Zafar M, Mahmood S, Shaikh H, Alhamidi A, Ramay SM, Saleem M, et al. Structural, dielectric and optical investigations of Zr incorporated ceria nanoparticles. *Mater Res Express.* 2019;6(11):116321. <https://doi.org/10.1088/2053-1591/ab4f28>
 105. Oh T-S, Boyd DA, Goodwin DG, Haile SM. Proton conductivity of columnar ceria thin-films grown by chemical vapor deposition. *Phys Chem Chem Phys.* 2013;15(7):2466–72. <https://doi.org/10.1039/c2cp43036c>
 106. Yamamoto T, Momida H, Hamada T, Uda T, Ohno T. First-principles study of dielectric properties of cerium oxide. *Thin Solid Films.* 2005;486(1–2):136–40. <https://doi.org/10.1016/j.tsf.2004.11.240>

SUPPORTING INFORMATION

Additional supporting information can be found online in the Supporting Information section at the end of this article.

How to cite this article: Steiner C, Hagen G, Kogut I, Fritze H, Moos R. Analysis of defect mechanisms in nonstoichiometric ceria–zirconia by the microwave cavity perturbation method. *J Am Ceram Soc.* 2023;106:2875–2892. <https://doi.org/10.1111/jace.18938>